

Accuracy of Simulated Data for Bifacial Systems with Varying Tilt Angles and Share of Diffuse Radiation

Hartmut Nussbaumer^{1,+}, Gaby Janssen², Djaber Berrian³, Bruno Wittmer⁴, Markus Klenk^{1,*}, Thomas Baumann¹, Franz Baumgartner¹, Marco Morf¹, Antonius Burgers², Joris Libal³, André Mermoud⁴

¹ Zurich University of Applied Science, SoE, Institute of Energy Systems and Fluid Engineering Technikumstrasse 9, 8401 Winterthur, Switzerland

² ECN.TNO, Solar Energy, Westerduinweg 3, 1755 LE Petten, The Netherlands

³ ISC Konstanz, Rudolf-Diesel-Str. 15, 78467 Konstanz, Germany

⁴ PVsyst SA, Route du Bois de Bay 107, 1232 Satigny, Switzerland

+ phone: +41 58 934 4799, + e-mail: hartmut.nussbaumer@zhaw.ch

* phone: +41 58 934 4804, * e-mail: markus.klenk@zhaw.ch (corresponding author)

Abstract Potential investors in bifacial PV systems are still deterred by the uncertainty of energy yield predictions. Validation of the prediction methods and establishing an accuracy range is therefore a central prerequisite concerning the bankability of the bifacial technology.

Because of the sensitivity on multiple additional factors compared to standard monofacial installations, the yield simulation of a bifacial PV array is far more complicated. The available simulation tools for bifacial systems still have to prove their reliability, also for predicting the effect of varying ambient and installation conditions. Moreover, bifacial devices enable new types of applications, such as vertical installations.

In this work, we compare the results of simulation tools developed at ISC Konstanz and ECN.TNO, as well as the output of the commercial PVsyst simulation software, to measured data. The measured data is obtained by a test rig that carries out a continuous and automated variation of the tilt angle. The test rig is not a single stand-alone module but an array in order to include shading effects of real extended systems. In addition, the measurements focus on a central module, which represents the conditions of a typical device in an array. Days with differing light intensity and share of diffuse radiation were chosen to determine the impact of the insolation conditions on the simulation accuracy. General trends with regard to the sensitivity to tilt and insolation conditions are analyzed in order to evaluate the quality of state-of-the-art bifacial energy yield simulations.

Keywords: bifacial, energy yield, measurement, simulation, accuracy, tilt angle

35 **Nomenclature**

36	αI_{sc}	Temperature coefficient I_{sc} [A.K ⁻¹]
37	β	Tilt angle (ground to module plane) [°]
38	γ	Ground reflection coefficient
39	ϵ	Clearness parameter in Perez model
40	$\varphi_{P_{max}}$	Bifaciality factor of the power ($P_{mpp, rear} / P_{mpp, front}$)
41	$\varphi_{I_{sc}}$	Bifaciality factor of the current ($I_{sc, rear} / I_{sc, front}$)
42	μV_{oc}	Temperature coefficient (open circuit voltage) [mV.K ⁻¹]
43	Θ	Angle of beam incidence [°]
44	Γ	Technology dependent diode quality factor
45	θ_z	Sun zenith angle [°]
46	$BG_{I_x, meas}$	Bifacial gain of the current (measured)
47	$BG_{I_x, sim}$	Bifacial gain of the current (simulated)
48	DHI	Diffuse horizontal irradiance [W.m ⁻²]
49	E^0	Irradiance at standard testing conditions: 1000 W.m ⁻²
50	E_{gap}	Energy gap [eV]
51	F_1	Perez coefficient
52	F_2	Perez coefficient
53	$G(\beta)$	Irradiance at tilt angle (β)
54	G_{front}	Averaged irradiance on module front side [W.m ⁻²]
55	G_{rear}	Averaged irradiance on module rear side [W.m ⁻²]
56	GHI	Global horizontal irradiance [W.m ⁻²]
57	I_L	Photogeneration current [A]
58	I_o	Dark saturation current [nA]
59	I_{sc}	Short circuit current [A]
60	$I_{SC, front}^{eff}$	Effective short circuit current (front side) [A]

61	$I_{SC,rear}^{eff}$	Effective short circuit current (rear side) [A]
62	P_{mpp}	Power at maximum power point [W]
63	R	Reflection coefficient
64	R_{series}	Series resistance [Ω]
65	R_{shunt}	Shunt resistance [Ω]
66	T	Transmission coefficient
67	U_c	Heat transfer coefficient [$Wm^{-2}.K^{-1}$]
68	V_{oc}	Open circuit voltage [V]
69	VF_x	View factor of module plane to x (x : <i>sky, ground</i>)

70

71 1. Introduction

72 Currently bifacial technology attracts considerable interest in the PV community and a constantly
73 increasing share of bifacial capacity is also expected for the future (VDMA-PV, 2019). Due to
74 technical progress, such as improved bifacial cell concepts or the availability of thin solar glass,
75 the technology gets increasingly attractive (Libal and Kopecek, 2018) (Nussbaumer et al., 2018)
76 (Osborne, 2017). Moreover, most of the advanced solar cell technologies, which are currently
77 implemented in industrial production, allow a comparatively simple adaption to a bifacial layout
78 (Romijn, 2017) (Veschetti, 2016). The interest in “peak shaving” and customized solutions for
79 specific applications, further supports the development towards bifacial technology (Faturrochman
80 et al., 2018) (Kreutzmann, 2017) (Guerrero-Lemus et al., 2016) (Soria et al., 2016) (Obara et al.,
81 2014) (Lim et al., 2014) (João, 2013) (Nordmann et al., 2012).

82 The potential for an increased power output of bifacial modules was demonstrated by simulations
83 and measurements on single modules or installations in various orientations (Libal and Kopecek,
84 2018) (Stein et al., 2017) (Appelbaum, 2016) (Ishikawa, 2016) (Reise and Schmid, 2015)
85 (Yusufoglu et al., 2015) (Van Aken et al., 2014) (Guo et al., 2013) (Sugibuchi et al., 2013) (Kreinin
86 et al., 2010). Nevertheless, potential investors in bifacial technology are often deterred by the
87 uncertainty of the yield predictions (Kopecek and Libal, 2018) (Meydbray, 2018), which is caused
88 by the considerably more complicated conditions compared to monofacial standard installations.

89 For freestanding bifacial modules, the optimum orientation is a trade-off between the front and
90 rear side irradiance and the efficiency is dependent on factors such as the ground reflectance or
91 the installation height. In real, extended systems, the arrangement of multiple modules has
92 additional effects, such as direct shading by modules in adjacent rows or indirect shading of the
93 modules surrounding, which results in a reduced effective albedo. Data of larger systems are rare
94 and the results are linked to a specific mounting and/or the respective orientation. Accordingly,
95 the generalization of field data from specific bifacial installations is difficult and the optimal
96 installation conditions or module orientations are not known with sufficient accuracy.

97 The simulation of bifacial systems is more complicated as compared to monofacial installations.
98 While the use of simulation tools is state-of-the-art and widely accepted to calculate the yield of
99 projected monofacial standard systems, their adaption for bifacial systems is still ongoing and their
100 reliability needs to be proven by comparison with measured data.

101 Several institutes and companies currently work on the development of suitable models,
102 algorithms and software for bifacial applications (Chudinzow et al., 2019) (Chiodetti et al., 2018)
103 (DiOrio and Deline, 2018) (Janssen et al., 2018) (Mermoud and Wittmer, 2018a) (Berrian et al.,
104 2017) (Dassler, 2017) (Gali, 2017) (Hansen et al., 2017) (Kunath, 2017) (Castillo-Aguilella and
105 Hauser, 2016) (Lindsay et al., 2016b) (Shoukry et al., 2016) ("Solarworld," 2016) (Reise and
106 Schmid, 2015) (Wang et al., 2015) (Yusufoglu et al., 2015).

107 These models use different approaches to simulate the amount of irradiance reaching the rear
108 side of a bifacial module, such as view factors, ray tracing, and empirical modelling (Liang et al.,
109 2019) (Pelaez et al., 2019) (Chiodetti et al., 2018) (Deline et al., 2017) (Marion et al., 2017)
110 (Castillo-Aguilella and Hauser, 2016) (Hansen et al., 2016) (Lindsay et al., 2016a) (Van Aken,
111 2016). The different approaches and algorithms vary in complexity and the prediction accuracy
112 may show a differing dependency on the relevant factors concerning the ambient and the
113 installation conditions.

114 The presentation of data obtained on a test array for the systematic measurement of bifacial
115 modules (Nussbaumer et al., 2019) (Baumann et al., 2017) (Klenk, 2017) sparked the interest of
116 groups, which work on corresponding simulation tools. In this work, the prediction accuracy of
117 these models is tested by a comparison of measured and simulated data. The focus of this work
118 is not the comparison of long-term measurement data with simulation results, but the simulation
119 of specific conditions. Days with different light intensity and share of diffuse radiation were chosen
120 to determine the impact of the irradiation conditions on the simulation accuracy. Front side and
121 rear side effects are respectively analysed and discussed. Due to the properties of the test rig, the
122 simulation validation is respectively possible for a tilt angle range from 0° to 90°. Accordingly, it is
123 possible to reveal irradiation and tilt angle related dependencies of the simulation tools.

124

125 **2. Measurement set-up**

126 The data acquisition is done on the BIFOROT (Bifacial Outdoor Rotor Tester), which enables a
127 continuous tilt angle variation. The BIFOROT is located on the roof of the ZHAW (Zurich University
128 of Applied Science) in Winterthur, Switzerland. It is a 3x3-module array for the systematic
129 measurement of bifacial systems with varying mounting conditions (Klenk, 2018) (Klenk, 2017)
130 (Baumann et al., 2017). This array is based on commercially available, 60-cell modules (Megacell,
131 MBA-GG60-270) with a nominal frontside power of 268 Wp and a bifaciality factor for the power
132 of 78 %. The basic set-up of the BIFOROT is depicted in Fig. 1, the implemented test rig is shown
133 in Fig. 2.

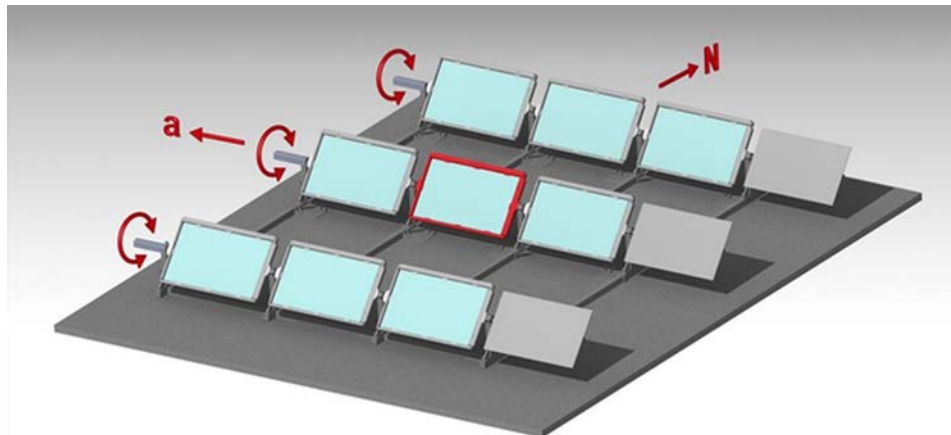
134 The most relevant device for this work is the bifacial module in the center of the 3x3 matrix, marked
135 red in Fig.1 and labeled as M2 in Fig. 2. This module in the center is best suited to represent the
136 shading situation for a typical location in an extended bifacial PV system. The benefit compared

137 to more common test set-ups with stand-alone modules, is the similarity to extended, real-world
138 installations with direct shading by other modules and indirect shading of the reflecting ground.
139 Additional shading elements are applied to one side, a further extension of the array was not
140 feasible due to the limited available space on the roof of the building.

141 Three rows of modules with manually adjustable distance between the rows are mounted on
142 vertically adjustable pillars. An important and unique feature of the BIFOROT is the automated
143 and continuous variation of the tilt angle in certain steps. In the experiments presented, twelve
144 angles in the range of 0° to 90° were selected. All panels change their tilt angle continuously and
145 coordinated with the central row. At each step an I-V curve of the center module M2 is measured
146 in order to get the power as a function of the tilt angle. One complete cycle is finished within one
147 minute. This allows the I-V curve measurement for different tilt angles at otherwise virtually
148 identical conditions and reveals the sensitivity of the simulations on the tilt. With 60 I-V curves and
149 P_{mpp} values per hour for each tilt angle position there are thus 720 I-V curves and P_{mpp} values per
150 hour. The P_{mpp} values can be summed over the course of the day to obtain the daily yield. The I-
151 V curve measurements of the BIFOROT is controlled by a LabView program. A set of load values
152 is respectively adjusted (Keysight N3305A, communication via Keysight 82357B interface) to
153 measure the I-V curves (Nussbaumer et al., 2019).

154 The BIFOROT includes several features to analyze bifacial system properties, such as
155 measurement of the rear side irradiation homogeneity, front and rear side measurements of
156 bifacial modules (modules M1, M3 in Fig. 2) and others. The modules M1 and M3 respectively
157 have a covered front and rear side in order to reveal the corresponding characteristics.

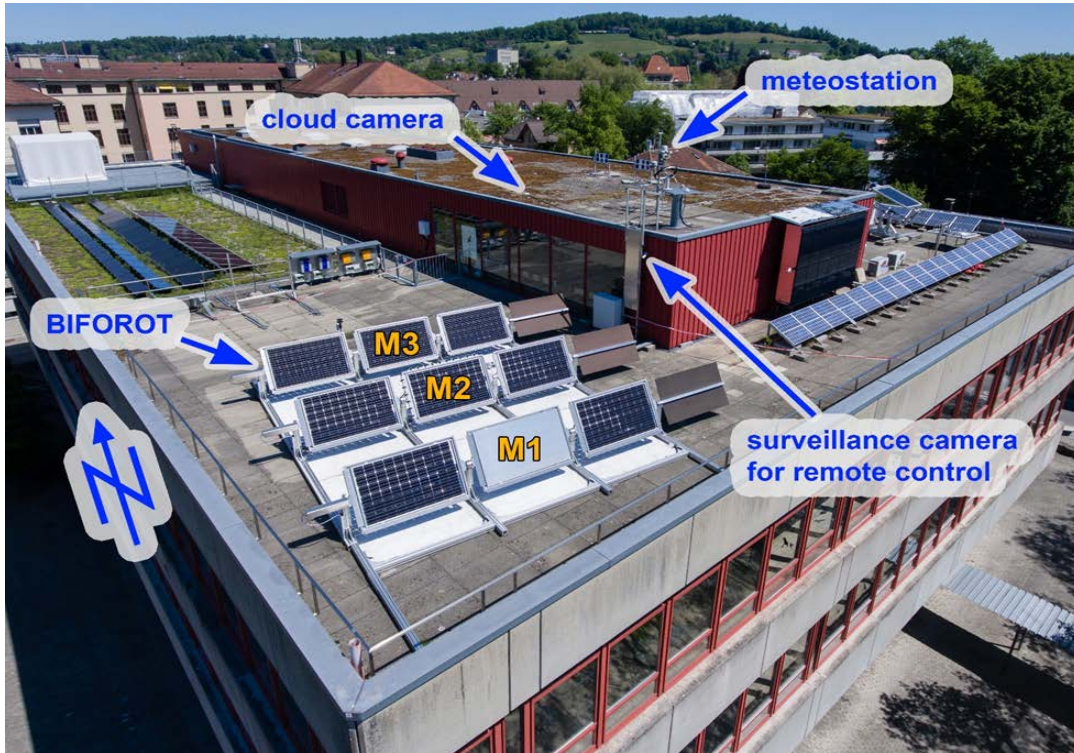
158



159

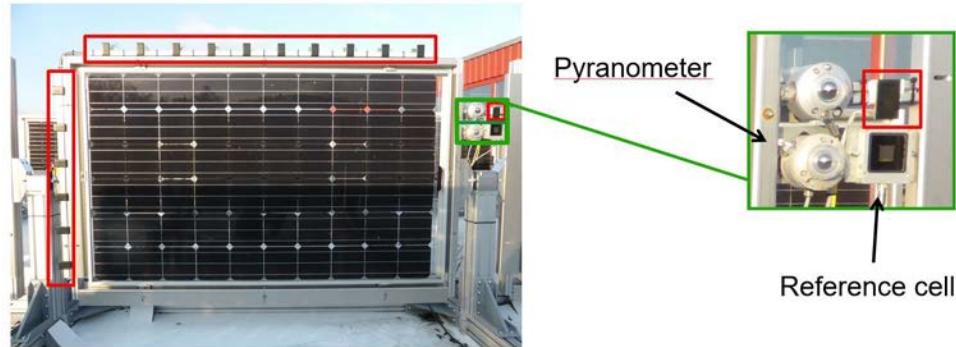
160 **Fig. 1.** Measurement set-up with permanently turning modules. The most relevant module in the
161 center, which is best suited to represent the actual conditions in real installations, is marked red.

162



163
164 **Fig. 2.** BIFOROT installation on the roof of the ZHAW in Winterthur. White reflecting roofing foil is
165 placed below the array. M1, M2 and M3 are similar bifacial modules. M1 has a covered front side,
166 M3 a covered rear side.

167
168 Weather data and environmental conditions are recorded by a meteorological station on the rooftop and by
169 measurement devices applied to the test rig. The meteorological station includes a pyranometer to measure
170 the global horizontal radiation, a horizontally mounted reference cell and a pyranometer with
171 shadow ring for the measurement of the diffuse radiation. Another pyranometer and reference cell
172 are mounted on the rotating mounting frame of module M2 as shown in Fig. 3. This pyranometer
173 has a relatively fast response time of 3s, in order to allow a good measurement for each constantly
174 changing tilt angle. The ambient temperature, the windspeed and other parameters are recorded
175 at the meteorological station, another temperature measurement is located at the test rig. In addition, the
176 V_{oc} characteristics of the modules can be used for a detailed temperature analysis.



179

180 **Fig. 3.** Reference cell and pyranometer (green frame), which both turn with the module plane of
 181 the device M2. The second depicted pyranometer was temporarily applied for comparative
 182 purposes. Small sensors (red frames), which are not used in this work are placed along the rim of
 183 the modules to determine the irradiation homogeneity (Baumann et al., 2017).

184

185 3. Simulation tools

186 The measured data is compared to computations carried out with the commercial simulation
 187 software PVsyst (V6.8.1) and simulation tools developed at ISC Konstanz and ECN.TNO. These
 188 three tools have in common that they are able to model the energy yield of both monofacial and
 189 bifacial PV systems for a fixed tilt or if mounted on trackers. The simulation tools need as input
 190 the weather data (ambient temperature and wind speed) as well as irradiance data i.e. global
 191 (*GHI*) and diffuse (*DHI*) horizontal irradiance. Typical for bifacial applications is that also an
 192 accurate estimation of the ground reflection coefficient (albedo) is required. Using the *GHI*, *DHI*
 193 and albedo an irradiance model is used to calculate the irradiance on front and rear of the panel.
 194 These irradiance data are then fed into models describing the thermal and electric behavior. All
 195 three simulation tools consist of three main sub-models: the optical model (irradiance model), the
 196 thermal model and the electrical model. The main differences between the simulation tools
 197 considered in this study are in the irradiance model, but there are also some differences in the
 198 thermal and electric models.

199 The ISC Konstanz simulation tool is called “MoBiDiG” which stands for Modelling of Bifacial
 200 Distributed Gain (Berrian et al., 2019) (Berrian et al., 2017) (Shoukry, 2015). MoBiDiG uses the
 201 thermal model that requires the nominal operating cell temperature (NOCT), the plane of array
 202 (POA) irradiance and the ambient temperature as inputs (Ross and Smokler, 1986). While the
 203 electrical model is based on one electrical diode equivalent circuit which has been solved using
 204 the Desoto model (De Soto et al., 2006). Regarding the optical model, the plane of the array on
 205 the front and rear side irradiance is composed of three main elements: the direct irradiance, the
 206 diffuse irradiance, and the ground reflected irradiance. The determination of front and rear
 207 irradiance due to the direct component is a straightforward geometrical calculation, which requires
 208 as input the position of the sun in the sky and the tilt of the PV module. However, in order to figure
 209 out how much diffuse irradiance contributes to the POA irradiance, MoBiDiG uses the Perez model
 210 (particularly with 1990 coefficients for the current work) that shows the most compelling results in

211 comparison to other existing models (Perez et al., 1993) (Perez et al., 1990) (Perez et al., 1987).
212 The ground reflected irradiance to the back side of the PV module are modeled with quasi 3D view
213 factor concept taking into account shaded and unshaded areas on the ground as well as the layout
214 of the PV system, i.e number of modules per row and number of rows. A detailed description of
215 the irradiance model has been carried out in our previous work (Berrian et al., 2017).

216 The irradiance model of BIGEYE V3 of ECN.TNO calculates the direct irradiance similarly to the
217 MoBiDiG tool. It also uses the Perez model with 1990 coefficients to distinguish between the
218 circumsolar and isotropic part of the diffuse irradiance. However, the necessary view factors of
219 the module front and rear plane to the sky are fully 3D and numerically calculated. BIGEYE also
220 calculates the non-uniform (i.e. affected by shading) distribution of direct and diffuse irradiance
221 received by the ground. The ground reflected irradiance is then calculated from the ground
222 reflection coefficient and the integrated irradiance received at each location of the ground
223 multiplied with the numerically calculated view factor between the plane of the module and that
224 location on the ground. Reflection loss increases at non-normal incidence are taken into account.
225 A description of the tool is given in (Janssen et al., 2018) (Burgers et al., 2018) (Janssen et al.,
226 2015). Because of the numerically calculated view factors, BIGEYE can take into account finite
227 lengths of arrays, variable inter-array distances and non-uniform tilt angles in a field. The thermal
228 model of BIGEYE (Lamers et al., 2018) is based on a simple stationary heat balance. The electric
229 model is a single-diode model. The temperature dependence of the photogeneration current I_L is
230 user-supplied, the temperature dependence on the diode ideality as well as the dark saturation
231 current I_0 is calculated as outlined by (De Soto et al., 2006), using the bandgap value for silicon of
232 1.12 eV. The total photogeneration is taken proportional to the front side irradiance augmented
233 with rear side irradiance multiplied by the bifaciality factor for the power, i.e. the equivalent or
234 compensated current method (Janssen et al., 2017).

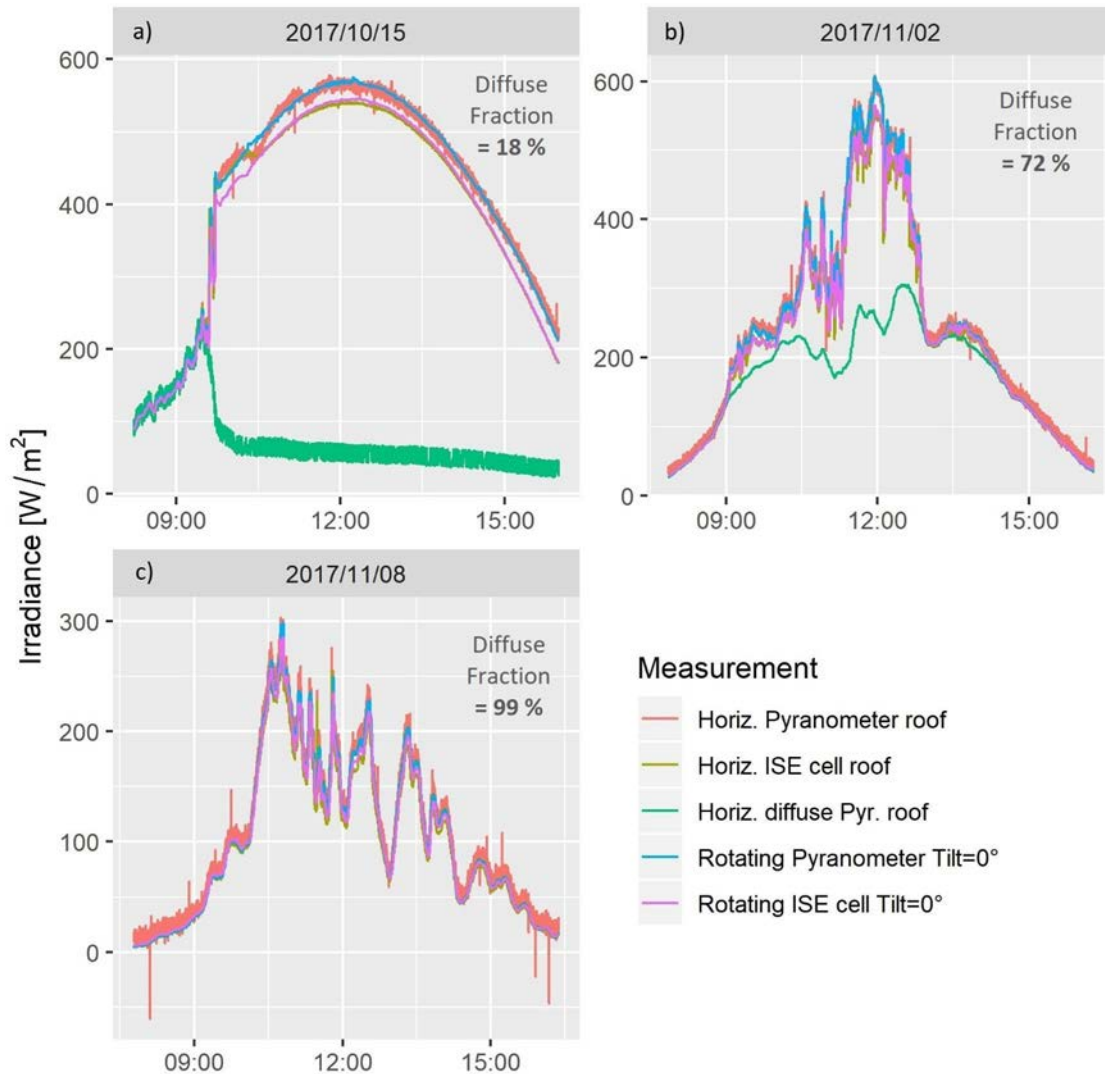
235 The commercial PVsyst simulation tool offers in its most recent versions also the option to simulate
236 bifacial systems. A model describing bifacial modules for fixed tilt installations with regular rows
237 was introduced in Version 6.6.0 (Mermoud and Wittmer, 2017), which was generalized to
238 horizontal single axis trackers in Version 6.7.0 (Mermoud and Wittmer, 2018a) (Mermoud and
239 Wittmer, 2018b). The approach calculates the front side irradiance like in a normal monofacial
240 simulation, and then adds the rear side contribution to it. This calculation includes ground
241 scattering to the front and backside of the modules, as well as direct and sky diffuse contributions
242 on the backside. The bifacial model assumes that the rows of PV modules all have the same
243 orientation and are spaced equally. In this way, the model can be fully described by a two-
244 dimensional cross section of the rows. This approximation is well suited for long regular rows as
245 they occur in large scale ground mounted PV installations, or on flat rooftop installations. Since
246 the experimental setup used in this work measures the center module, which is representative for
247 modules inside a long row, the 2D bifacial model becomes a good approximation. Once the rear
248 side irradiance has been calculated, the bifaciality factor of the PV module is applied to it. The
249 result is added to the front side irradiance and then used as input for the single diode model that
250 is used by PVsyst.

251 Details to the simulation parameters, which were used in the respective simulation tools, can be
252 found in the Appendix – Simulation parameters.

253

254 **4. General aspects**

255 In this study, measured and simulated data are compared in order to determine the resulting
256 accuracy and to reveal specific trends. Three days from October and November 2017 with differing
257 insolation intensity and share of diffuse radiation were chosen (Fig. 4). While the 10/15/2017
258 represents almost clear sky conditions, the 11/08/2017 is a completely overcast day with negligible
259 direct insolation. As an example for a day with mixed conditions, the 11/02/2017 was selected.
260 The aim of this approach is to reveal the specific properties of the respective simulations with
261 regard to the irradiation conditions and tilt angles.

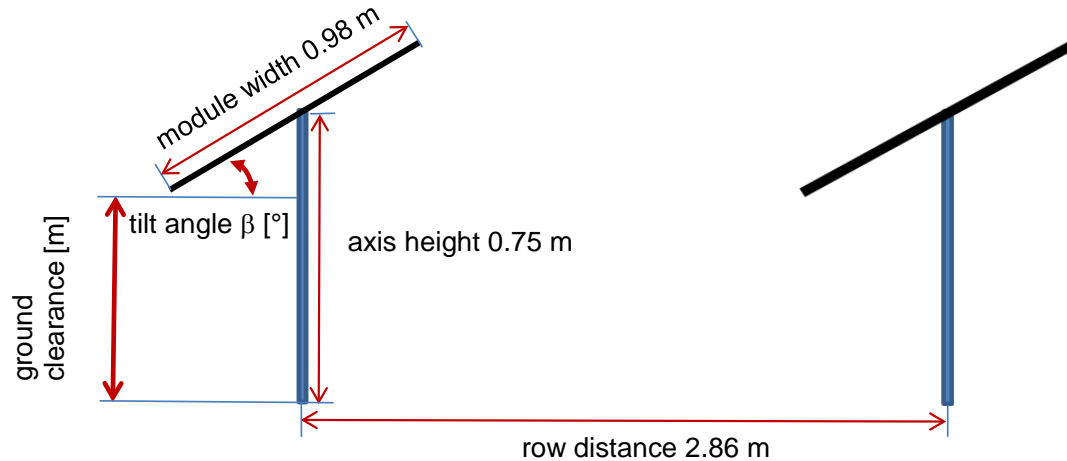


262
263 **Fig. 4.** Three days with differing insolation intensity and share of diffuse radiation, ranging from
264 an almost clear sky (10/15/2017, diffuse fraction: 18 %, Fig. 4a)), mixed irradiation conditions
265 (11/02/2017, diffuse fraction: 72 %, Fig. 4b)) to a completely overcast day (11/08/2017, diffuse
266 fraction: 99 %, Fig. 4c)), were chosen for the analysis. The measurement data of the sensors on
267 the roof and of the rotating sensors at the BIFOROT at 0° tilt are shown.

268

269 The dimensions, distances and angles as used in the experimental setup are schematically
270 depicted in Fig.5. The row distance is 2.86 m, the module width 0.98 m. Due to the fixed height of
271 rotational axis at 0.75 m the module height, typically defined by the ground clearance, the distance
272 of the lower module edge to the ground, is varying.

273



274

275 **Fig. 5.** Schematic drawing of the relevant dimensions, angles and distances. During the
276 measurements, the row distance was kept constant at 2.86 m as well as the axis height (0.75 m).

277

278 To obtain an increased albedo compared to the concrete ground a white roofing foil was placed
279 beneath the test rig as shown in Fig.2. During the measurements that are presented in this work,
280 the foil was moderately soiled and in a condition that is typical for several weeks of outdoor use.
281 Even though a certain variation of the albedo was observed in extended measurements, a
282 constant albedo factor of 0.51 was used in all models.

283 The site used in the simulation is located at 47.50° N and 8.73° E, at 440 m above sea level. No
284 horizon profile was applied in the simulations.

285

286 5. Simulation results

287 The output of bifacial modules is combined from the front and rear side contribution. It is therefore
288 of interest to consider the respective contributions if the accuracy of simulations is investigated.
289 The BIFOROT enables such an analysis by its setup.

290 The results that will be discussed here are

- 291 ▪ Calculated front side irradiance compared to data of a pyranometer on the module axis
292 (M2). The front side irradiance is also compared to the I_{sc} measured in M3.
293 ▪ The rear side irradiance as determined by the I_{sc} difference of the modules M3 and M2 or
294 directly by the I_{sc} of M1.
295 ▪ Power output measured in M2.

296
297 Simulations were done for all timestamps where data were available, with appropriate
298 meteorological data at that timestamp. The simulation results include the power at each timestamp
299 and all contributions to the front and rear side irradiance at each timestamp. Data on the current
300 and voltage at the maximum power point are also available but will not be discussed here.

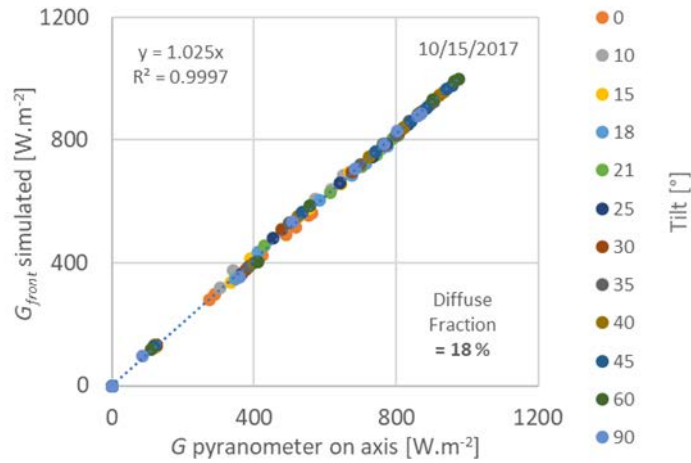
301
302 *5.1 Front side irradiance*

303 *5.1.1 Front side irradiance compared to pyranometer data*

304 The simulation of the front side irradiance is well established in the simulation of monofacial
305 modules. Nevertheless, tilt angles that can be a reasonable choice for bifacial installations also
306 include conditions that are rarely applied to monofacial systems. In the course of the data analysis,
307 the sensitivity of the output at specific conditions (low irradiation and steep tilt angle) to the
308 irradiation measurement was highlighted and is presented here.

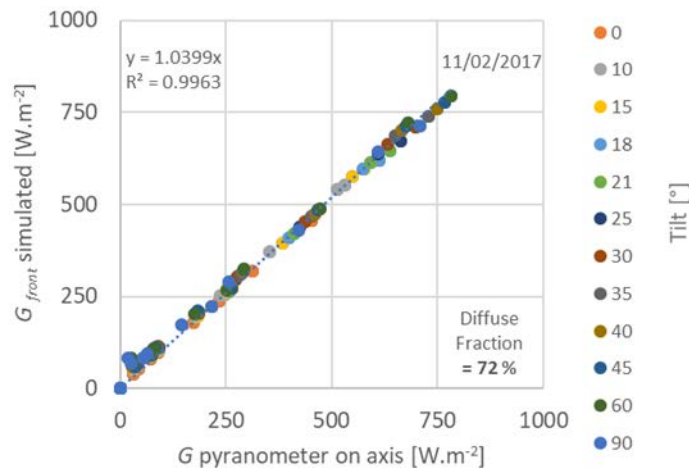
309 Fig.6 shows the correlation between the simulated front side irradiance on the module plane and
310 the irradiance measured with a pyranometer on the module axis. The simulated irradiance is the
311 average over the module plane, but note that on the days considered the front side irradiance was
312 essentially homogeneous. Only during the morning and evening hours and for steep tilt angles
313 direct shading occurred. In Fig. 6 data from ECN.TNO is presented exemplarily, the results from
314 the other groups are very similar. Note that for this comparison the simulated irradiance does not
315 include the angular loss coefficient. The simulation is based on measured GHI and DHI irradiance
316 data obtained by pyranometers with and without shadow ring on the roof (see also eq. (1) further
317 below). The plotted data are hourly averages of the simulated results and measured data. The fit
318 results correspond to a line through all data with intercept zero. The correlation of the data plots
319 is very good with slopes close to one, except for the example at completely overcast conditions
320 (11/08/2017).

321



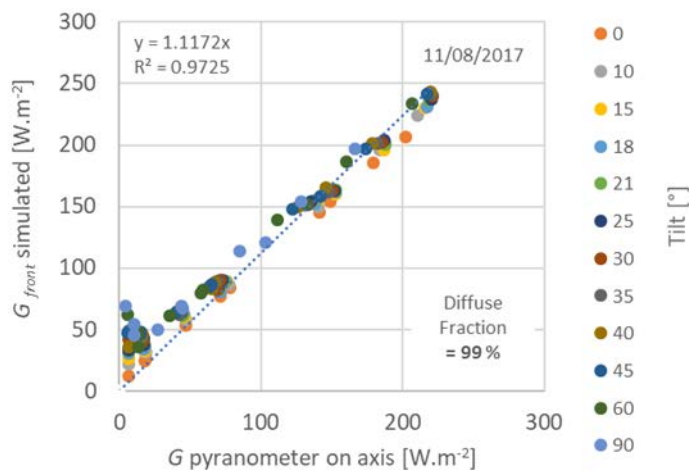
322

a)



323

b)



324

c)

325 **Fig.6.** Measured and simulated irradiance (hourly average) on the front side of M2. The measured
 326 irradiance (x-axis) is recorded with the pyranometer on the module axis. The basis for the
 327 simulations is the irradiance measured with the pyranometer on the roof, transposed to the
 328 respective tilt angles, which are identified by spots of different colors. Calculations with BIGEYE.

329

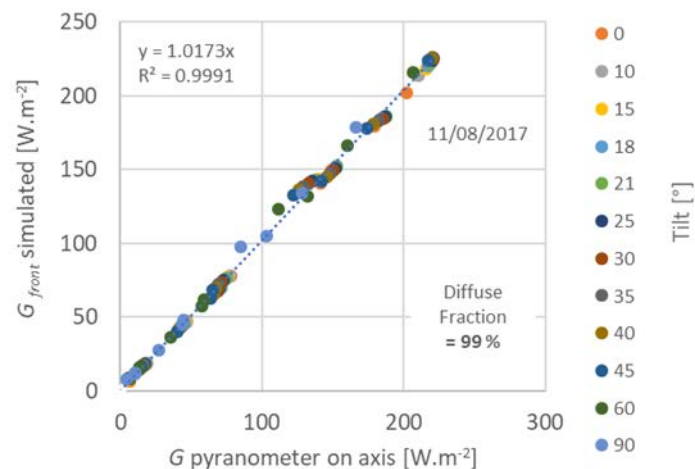
330

331 The deviation that occurred when performing the data evaluation for the covered day on
332 11/08/2017 was thus analyzed in more detail. The irradiation data for the simulations shown in
333 Fig.6 was measured with the pyranometer on the roof. Even though there is an apparently good
334 similarity between the irradiation data from both pyranometers (see Fig.4 c)), the simulation was
335 again performed with the data of the rotating one at 0° tilt angle.

336 The integrated, simulated G_{front} on a plane with zero tilt angle for that day was 943 Wh. The
337 integrated irradiance of the rotating pyranometer at zero tilt was only 894 Wh, i.e. a 5 % deviation.
338 A check showed that on 11/08/2017 the total, integrated irradiation measured by the pyranometer
339 on the roof was 949 Wh, i.e. within 0.6 % of the simulated result. This indicates that the
340 discrepancy is not due to the irradiance model or its implementation in the used simulation
341 (BIGEYE) but due to a significant discrepancy (5 %) between the readings of the two
342 pyranometers. The different readings can for example be caused by shading, particularly of the
343 rotating pyranometer in the test array, that can affect the measured values and that may also show
344 an angular dependency.

345 In view of this discrepancy, another simulation was done using the zero tilt data of this rotating
346 pyranometer for all angles (this means a difference in timestamp between meteorological data
347 and module results of less than 1 minute). Fig.7 shows that with this approach the agreement is
348 much better for all angles.

349



350

351 **Fig.7.** In spite of the apparently good congruence of the irradiation data (Fig.4c)) from both
352 pyranometers, the agreement for overcast conditions (11/08/2017) is significantly improved
353 (compare to Fig. 6c)) if the irradiance data from the rotating pyranometer at 0° tilt angle is used.
354 Calculations with BIGEYE.

355

356 The 'rotating pyranometer' gives lower GHI , and therefore lower beam component ($GHI-DHI$), and
357 a lower clearness parameter ϵ for the Perez model (Perez et al., 1993) (Perez et al., 1990) (Perez
358 et al., 1987). According to the Perez model, the irradiance on a plane with tilt angle β is given by:

359

360 $G_{front} =$

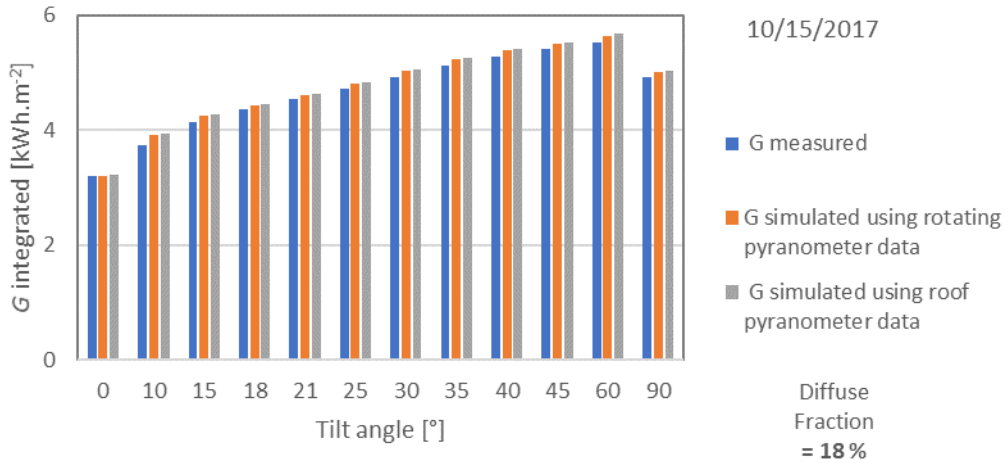
361
$$(GHI - DHI + DHI \cdot F_1) \frac{\cos \theta}{\cos \theta_z} + DHI \cdot [(1 - F_1) \cdot VF_{sky} + F_2 \cdot \sin \beta] + \gamma \cdot GHI \cdot VF_{ground} \quad (1).$$

362

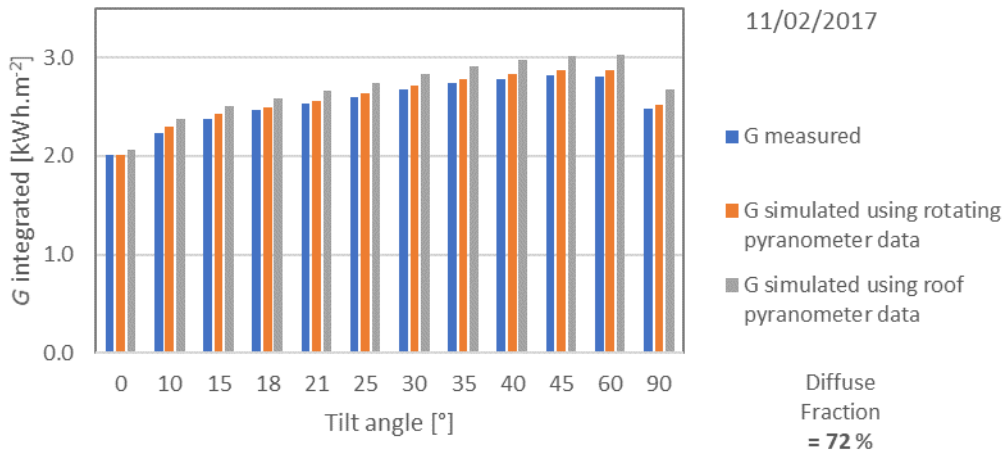
363 Here θ is the angle of beam incidence, θ_z the sun zenith angle and γ the ground reflection
364 coefficient. F_1 and F_2 are Perez coefficients depending on ϵ and the sky brightness. At horizontal
365 tilt the ratio $\frac{\cos \theta}{\cos \theta_z}$ is one, but it increases with tilt until it reaches a maximum, which is at 11/08/2017
366 at about 60° . The view factor of the plane to sky decreases with the tilt angle. Any uncertainty in
367 the horizontal beam component ($GHI-DHI$) or in F_1 , the parameter determining the circumsolar
368 fraction, will be magnified at larger tilt angles, i.e. from a mere 5 % uncertainty in G_{front} at zero tilt
369 to 40 % at 90° , as shown in Fig.8.

370 It is also apparent from Fig. 8 that the relative deviation is strongly dependent on the irradiation
371 and that it is considerably more pronounced for conditions with low irradiance. These results show
372 how sensitive simulation results can be to the quality of the horizontal irradiance input at cloudy
373 days with low horizontal beam component ($GHI-DHI$). In the case of 10/15/2017, the beam
374 component prevails and both pyranometers give very similar readings. Uncertainties in the beam
375 component, and accordingly in the total irradiance, are therefore very small. Fig. 9 shows the
376 respective deviations, (simulated-measured) to measured, of the calculated front side irradiance
377 G for all three simulation tools for the selected days with varying irradiance conditions. In all
378 following calculations, the GHI values from the rotating pyranometer at the axis at zero tilt were
379 used for the simulations.

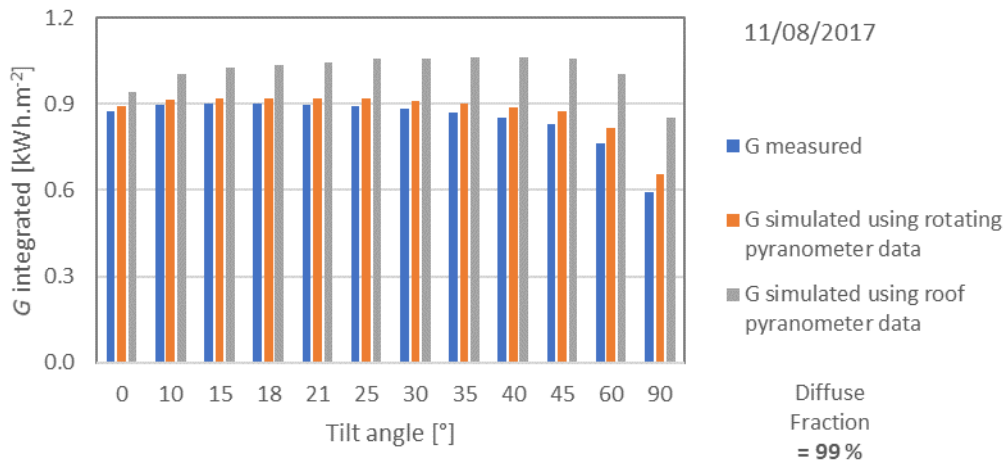
380



381 a)



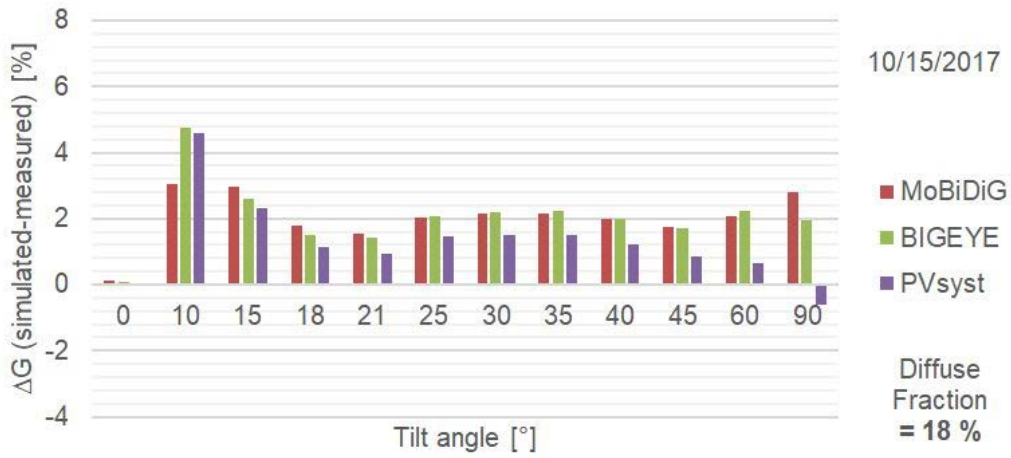
382 b)



383 c)

384 **Fig.8.** Integrated irradiance from measurement and the two simulations with different pyranometer
 385 data. Any uncertainty in the horizontal beam component ($GHI-DHI$) or in F_1 , the parameter
 386 determining the circumsolar fraction, will be magnified at larger tilt angles. The relative error
 387 increases for conditions with low irradiance. Calculations with BIGEYE.

388



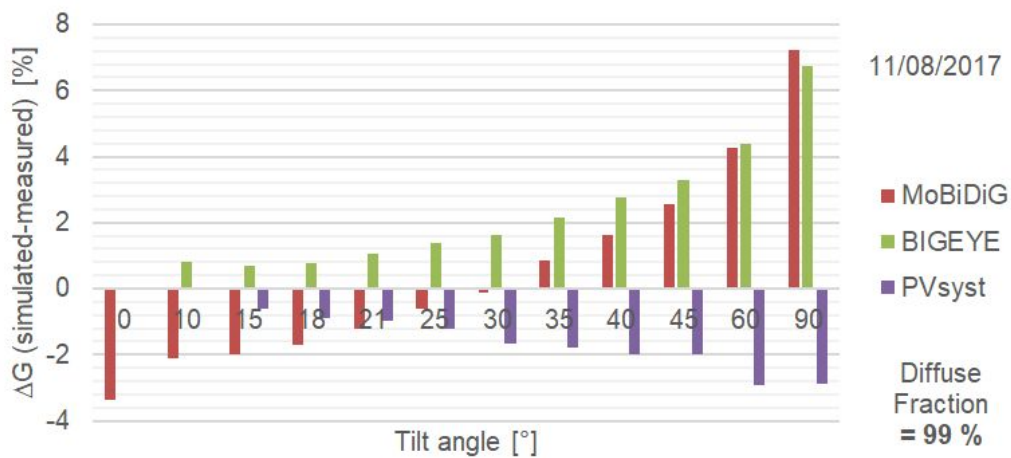
389

a)



390

b)



391

c)

392 **Fig.9.** Deviation, (simulated-measured) to measured, of the total front irradiation G at all tilt angles
 393 on all days.

394

395 5.1.2 Front irradiance compared to I_{sc}

396 Similar to the approach shown in Fig. 6 and Fig. 7 the BIFOROT also allows to correlate the I_{sc} of
397 M3, the bifacial module with covered rear side, and the front irradiance G . Like for the irradiance,
398 there is a good linear correlation. In contrast to Fig. 6 and Fig. 7 now also the tilt angle dependency
399 is analyzed by the use of the tilt angle dependent $G(\beta)$. By extrapolating the slope of the correlation
400 to STC irradiation conditions an effective I_{sc} for the front side can be calculated at each tilt angle:

401

$$402 \quad I_{sc}(M3, \beta) = I_{sc,front}^{Eff} \frac{G(\beta)}{E^0} \quad 2).$$

403

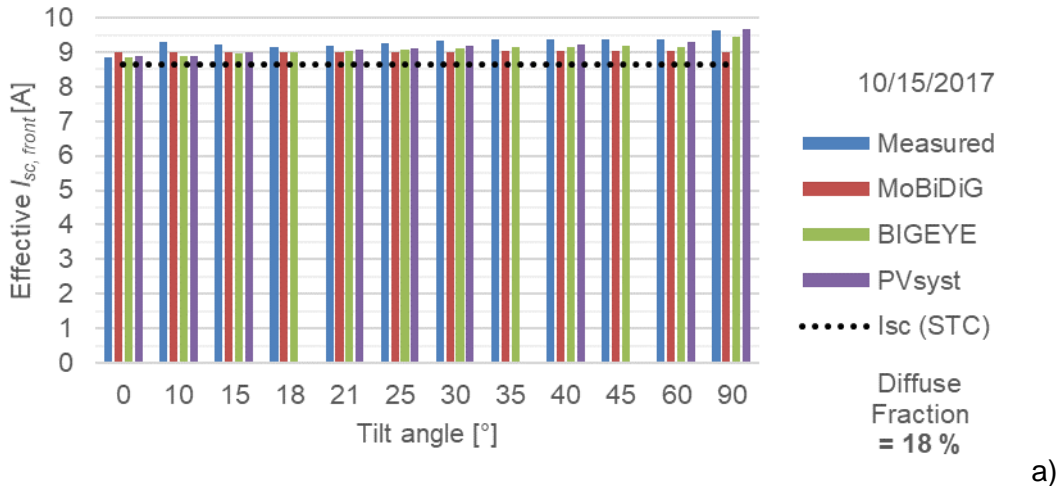
404 E^0 is the STC irradiance of $1000 \text{ W}\cdot\text{m}^{-2}$. For $G(\beta)$ we use the measured front side irradiance or the
405 simulated front side irradiance at tilt angle β , leading to 'measured' and 'simulated' $I_{SC,front}^{eff}$,
406 respectively.

407

408 Fig. 10 shows that the simulated data and measured data are in good agreement with each other.
409 This was already expected because of the good agreement of measured and simulated irradiance
410 shown in Fig. 9. The measured results are in fair agreement with the STC $I_{SC,front}$ of 8.65 A.
411 Deviations are expected because:

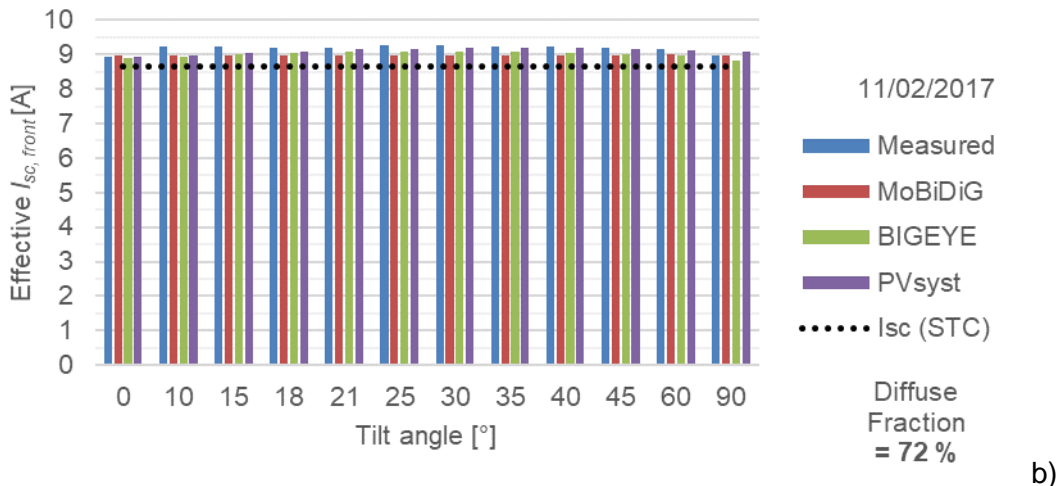
- 412 1) The module will have additional reflection losses because the angle of incidence is larger
413 than zero (angular loss coefficient is non-zero). Hence, the irradiance received by the
414 module is less than seen by the pyranometers. This would lead to effective $I_{SC,front}^{eff}$ values
415 smaller than the STC value, and varying with the tilt angle and timestamp. The data in
416 Fig. 10 do not suggest that the angular loss coefficient plays a major role here.
- 417 2) The generated current increases slightly with temperature ($3\text{-}4 \text{ mA}\cdot\text{K}^{-1}$). This effect should
418 be similar for all tilt angles and would lead to higher effective $I_{SC,front}^{eff}$. Note that the
419 BIFOROT rotation speed is so high that the actual cell temperature will be the effect of the
420 irradiance average overall tilt angles. The measured values are usually larger than the
421 STC values but the deviations are often larger than expected because of temperature
422 alone, with module temperatures in the range of $5\text{-}35 \text{ }^\circ\text{C}$.
- 423 3) Inaccuracies in the measured irradiance and current. The fact that the measured $I_{SC,front}^{eff}$
424 is always larger than the STC value indicates an underestimation of G or an overestimation
425 of the front side current.
- 426 4) The irradiance distribution on the module is not uniform. The cell with smallest irradiance
427 will limit the current leading to smaller measured currents.

428



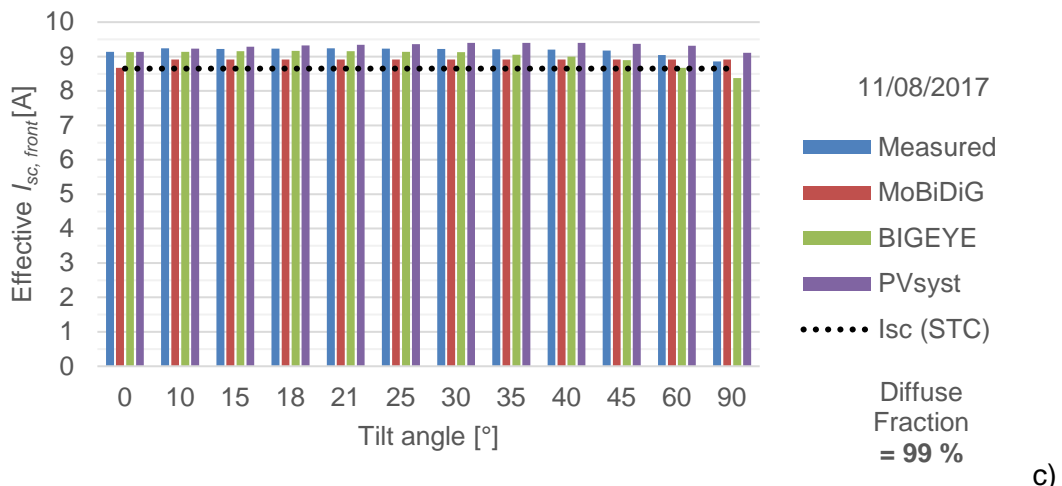
429

a)



430

b)



431

c)

432 **Fig.10.** Measured and simulated effective $I_{sc, front}$. The dotted horizontal line represents the STC I_{sc}
 433 value of 8.65 A measured indoors.

434

435

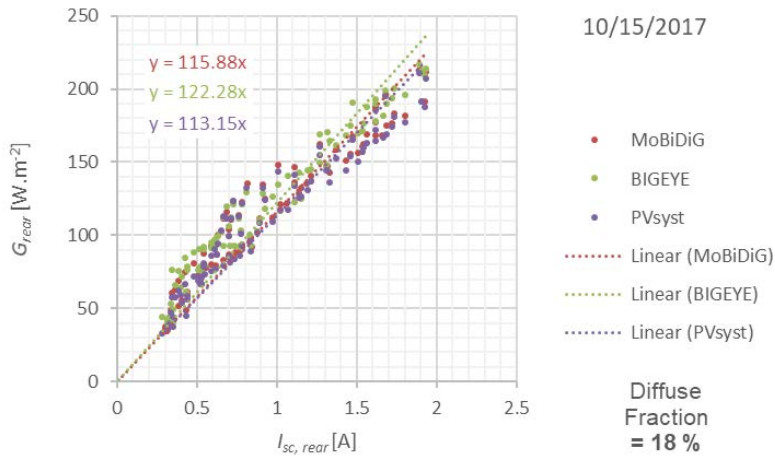
436 5. 2 Rear side irradiance

437 The rear side irradiance can be correlated to the I_{sc} of rear side sensitive module M1 or to the I_{sc}
438 difference of the modules M3 and M2 (front side sensitive and bifacial module). While the first
439 option is obviously more direct it turned out that the measurement results of the rear side alone
440 are more prone to additional shading effects and the errors resulting hereof. As a result, there is
441 always a certain difference between the I_{sc} as determined by these options (Klenk, 2017). During
442 the relevant measurement period, there was also an additional issue with the front row insolation.
443 A construction crane erected close to the BIFOROT caused a shading of the front row area and
444 resulted in pronounced ground shading below M1. At conditions with strong direct irradiance, this
445 shading affected the output of M1 considerably. Consequently, the rear side data obtained by M1
446 for the 10/15/2017 was erroneous, data between 12 PM and 3 PM would have to be omitted.
447 Therefore, it was decided to define the rear side I_{sc} for the simulations by the I_{sc} difference of M2
448 and M3. Figure 11 shows the simulated G_{rear} of the three simulation tools as a function of the
449 $I_{SC, rear}$. G_{rear} is averaged over the plane of the module by all three tools, more information can be
450 found in the appendix.

451 There is an overall linear relationship but it is clear that more deviations from linearity occur than
452 between front side measured and simulated irradiance (Figs. 6 and 7). Also, the differences
453 between the three tools become apparent. This reflects the complexity of the calculation of the
454 rear side irradiance, and the different choices made in the simulation codes.

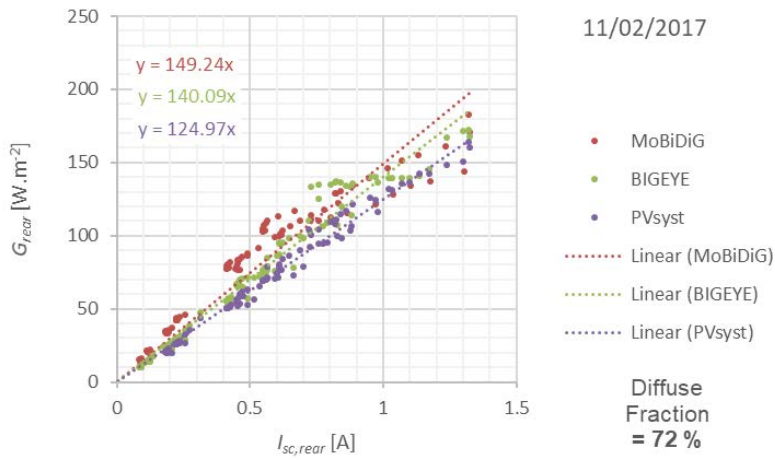
455

456



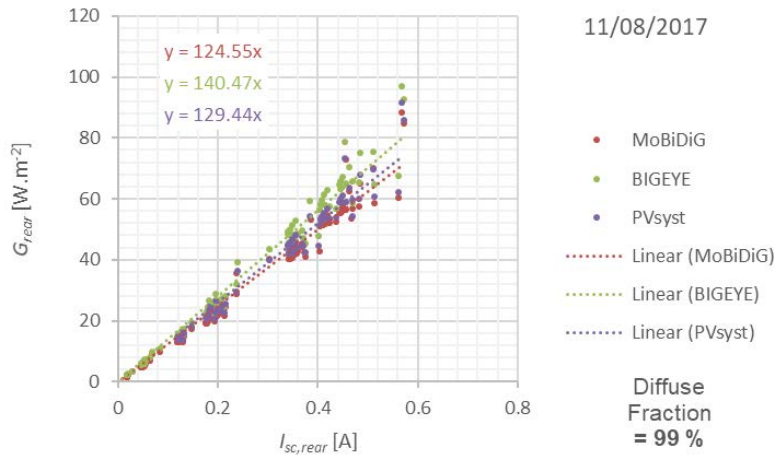
457

a)



458

b)



459

c)

460 **Fig.11.** The simulated rear side irradiance is compared to the measured rear side I_{sc} determined
 461 by the I_{sc} difference of M2 and M3. The correlation graphs of the selected days are shown for all
 462 three tools. The respective tilt angle of the data points is not indicated to reduce the complexity.

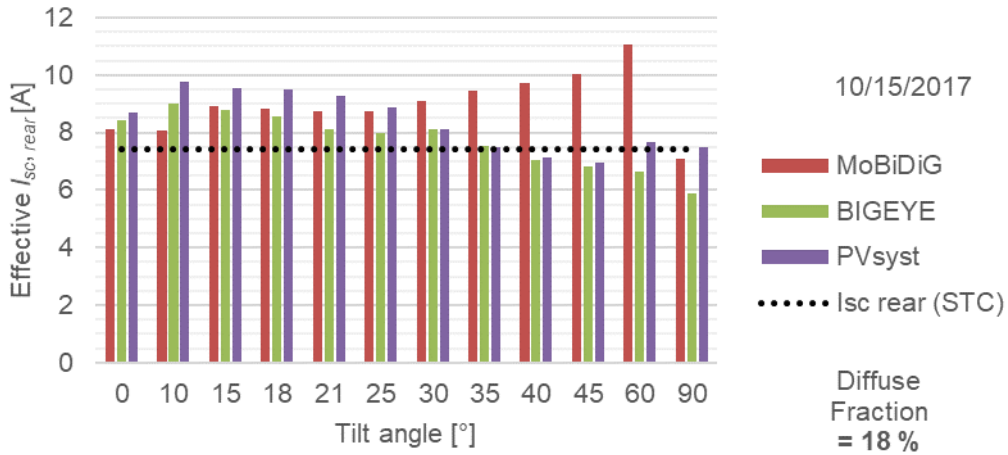
463

464 Tilt-angle resolved comparisons can be made from Figure 12. As was done for the front side
465 (eq. 2) effective I_{sc} values can be calculated: using

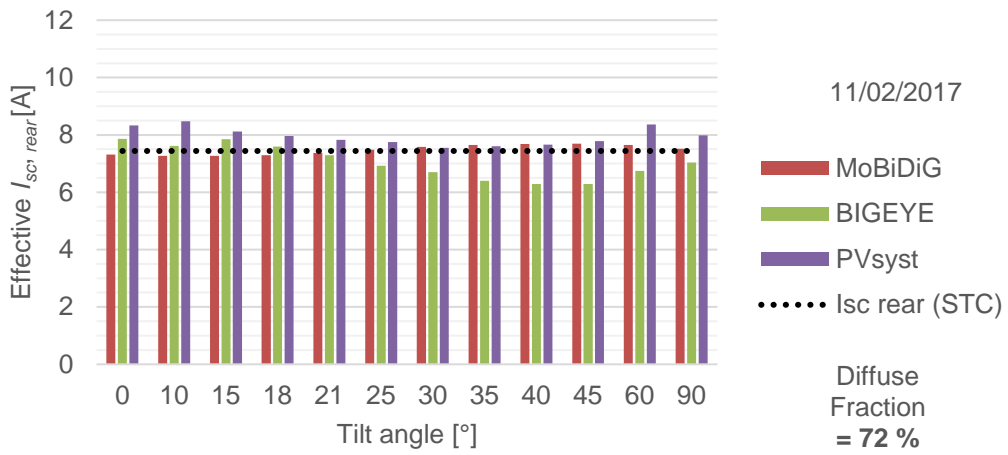
466
$$I_{sc}(M2, \beta) - I_{sc}(M3, \beta) = I_{sc, rear}^{Eff} \frac{G_{rear}(\beta)}{E^0} \quad (3).$$

467
468 The comparison is now with the rear STC value of 7.44 A. Again, temperature effects and angular
469 dependent reflection have to be allowed for. Values of $I_{sc, rear}$ that are significantly larger than the
470 STC values are an indication that the simulation underestimates the irradiance on the rear or that
471 the difference of the I_{sc} in M2 and M3 is overestimating the contribution of the rear side to I_{sc} .
472 Figure 12 shows that values both substantially higher and lower than the STC value are found.
473 The highest values were obtained with the PVsyst data, in agreement with the lower rear
474 irradiance values shown in Figure 11. There does not seem to be a strong correlation with the tilt
475 angle or the day (i.e. irradiance conditions), although the most variation in $I_{sc, rear}^{Eff}$ was found on the
476 day with the highest beam component. Note, that the ratio of the $I_{sc, rear}^{Eff}$ and effective $I_{sc, rear}^{Eff}$
477 represents an effective bifaciality factor for the current.

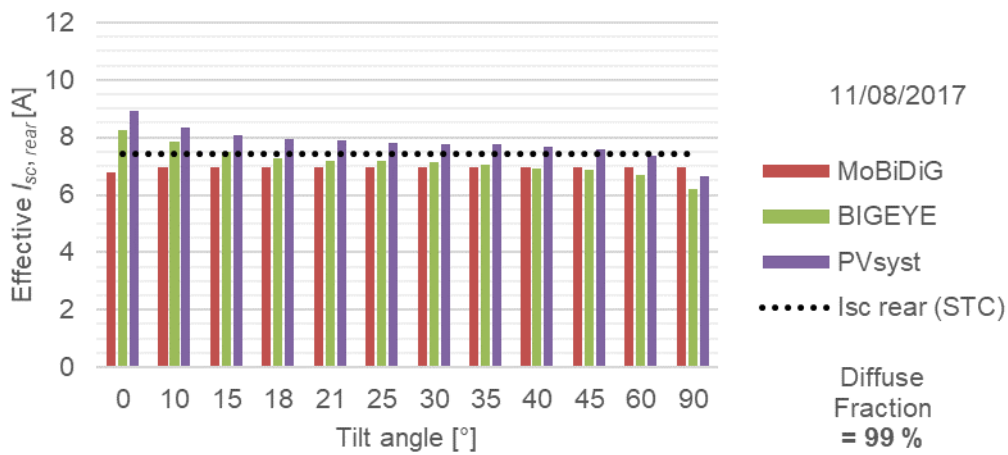
478



479 a)



480 b)



481 c)

482 **Fig.12.** Effective $I_{sc, rear}$ calculated using irradiance on the rear side of M2. The dotted horizontal
 483 line represents the STC value.

484

485 5.3 Bifacial gain in the current

486 The comparison of calculated and measured bifacial gain in the power would require a
487 comparative power measurement of the bifacial module M2 and the front side sensitive module
488 M3. However, during the presented measurements only I_{sc} measurements were implemented for
489 the front and rear side sensitive modules M2 and M3. The recording of the full I-V curve, and thus
490 of the power, was only available for the bifacial module M2. Therefore the bifacial gain of the
491 current was analyzed instead of the more common bifacial gain of the power.

492

493 The bifacial gain in the current BG_I can be calculated as:

494
$$BG_{I,meas} = \frac{I_{sc,rear}}{I_{sc,front}} \quad (4)$$

495 This measured value was calculated by integrating the currents over the whole day at each tilt
496 angle and then taking the ratio. The simulated values were calculated from:

497
$$BG_{I,sim} = \frac{G_{rear}}{G_{front}} \cdot \varphi_I \quad (5)$$

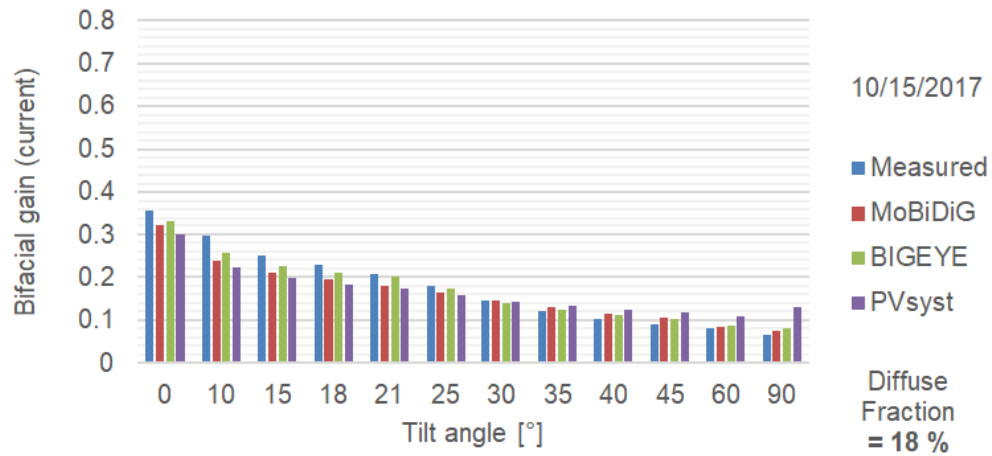
498 Here φ_I is the bifaciality factor for the current. i.e. the ratio of the rear and front STC values of the
499 I_{sc} obtained in previous indoor measurements.

500
$$\varphi_{Isc} = 7.44 / 8.65 = 0.86 \quad (6)$$

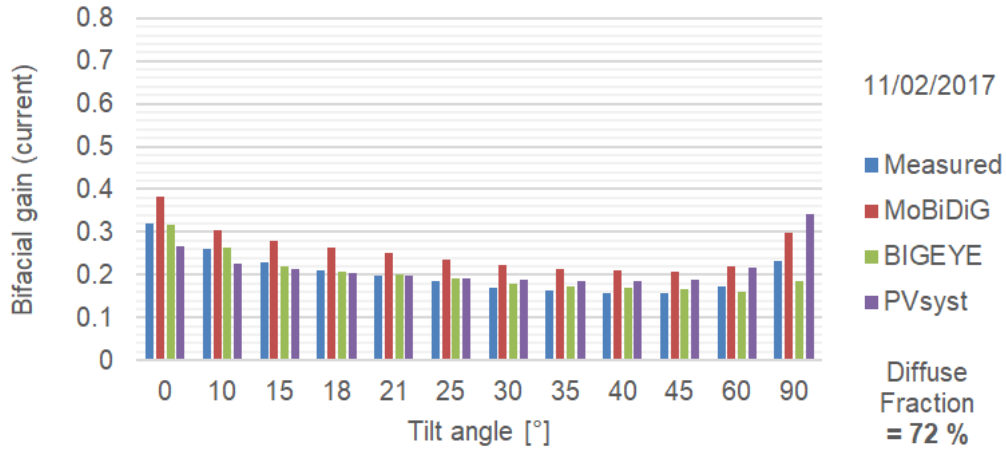
501 Fig. 13 shows that the simulations reflect the trend in bifacial gain quite well. The measured bifacial
502 gain strongly depends on the tilt angle and the irradiance conditions. For clear sky conditions there
503 is a decrease in gain with tilt angle and an increase for the day where diffuse light predominates.

504

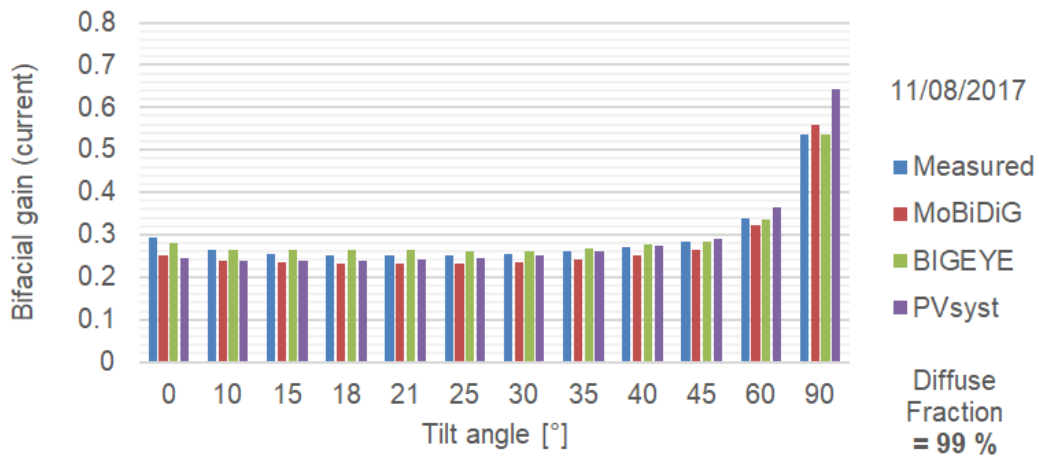
505



506



507



508

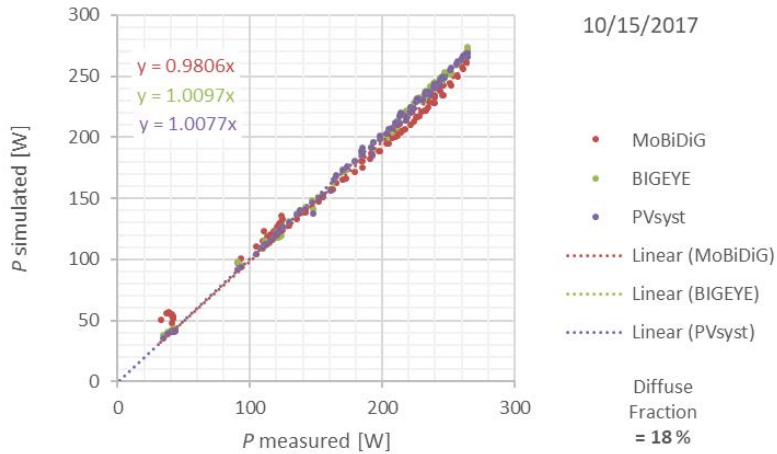
509 **Fig.13.** The effective bifacial gain of the current from measured I_{sc} data and from simulated
510 irradiance data with an assumed bifaciality value of the current of 0.86. The calculated data is
511 compared for all three simulation tools.

512

513 5.4 4 Power output

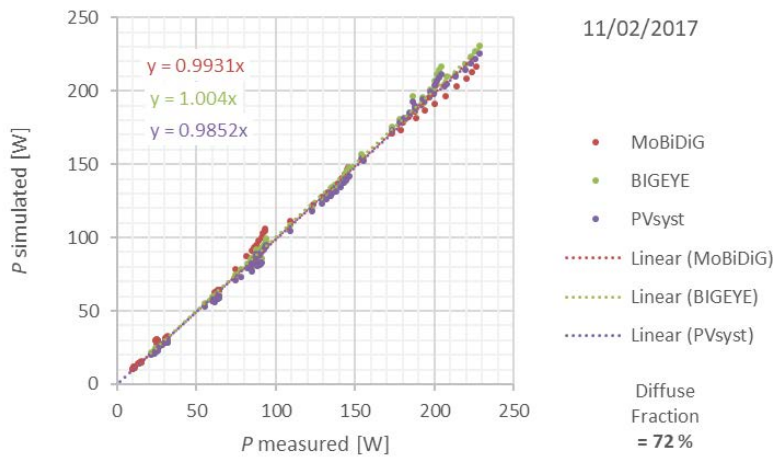
514 The power output can be directly compared to the measured output. In the simulations, the power
515 bifaciality factor $\phi_{Pmax} = 0.78$ was used to calculate the current enhancement. The correlation
516 graphs are shown in Fig. 14. The correlation is very good, leading to slopes very close to one.
517 Note, that the power output also includes effects of temperature and of the specifics of the I-V
518 curve.

519



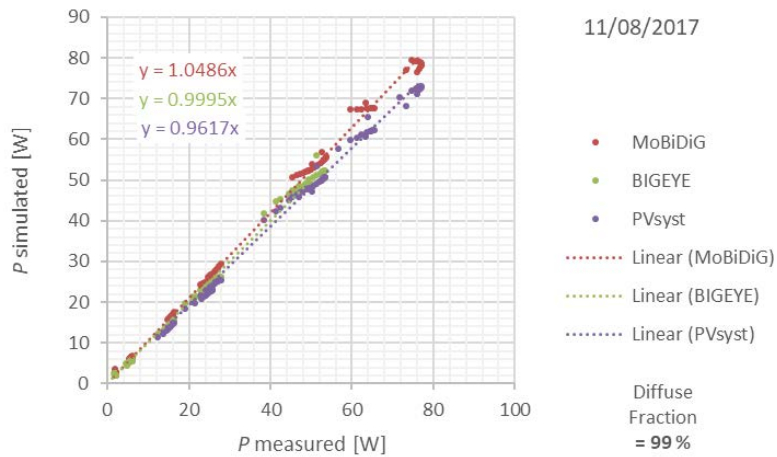
520

a)



521

b)



522

c)

523 **Fig. 14.** Direct comparison of the simulated and measured power output for all three tools. In the
 524 simulations, the power bifaciality factor was used to calculate the current enhancement. The
 525 respective tilt angle of the data points is not indicated to reduce the complexity.

526

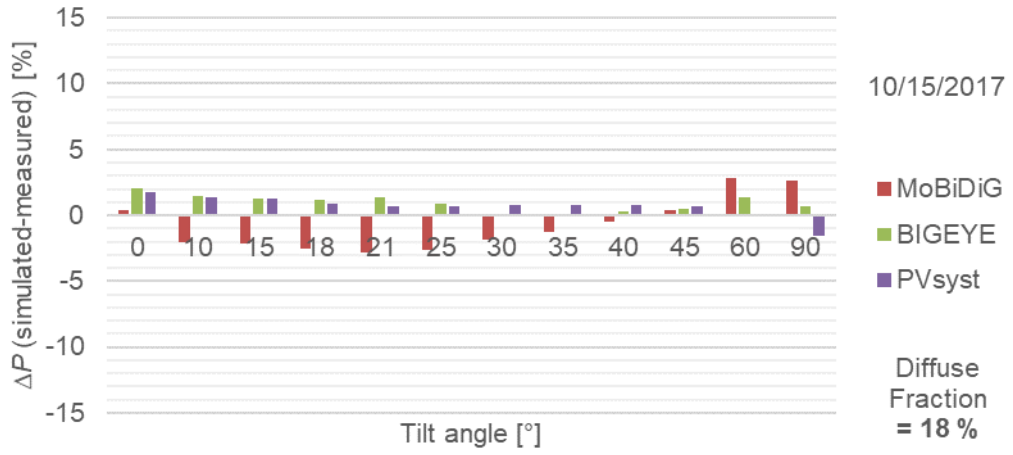
527 Fig.15 shows the deviations in integrated power output, (simulated-measured) to measured, for
528 all tilt angles at all days. Particularly for conditions with high direct irradiance share (10/15/2017),
529 the deviations are remarkably small. For this day, the course over the tilt angles shows a
530 characteristic dip for moderate tilt angles. For 30° to 45° the deviation is smaller than $\pm 2\%$ for all
531 models and mostly well below $\pm 1\%$. There is an increase of the deviation towards horizontal and
532 vertical tilt for these irradiation conditions, but the deviation is within $\pm 3\%$.

533 Larger deviations were found for conditions with low direct irradiance. Again, the largest deviations
534 are observed for horizontal and vertical tilt. For the conditions with low direct irradiation, the course
535 of the deviations show an increasing trend towards steeper tilt angles. There is also an "offset"
536 between the models; the maximum deviation can be found at horizontal or vertical mounting.

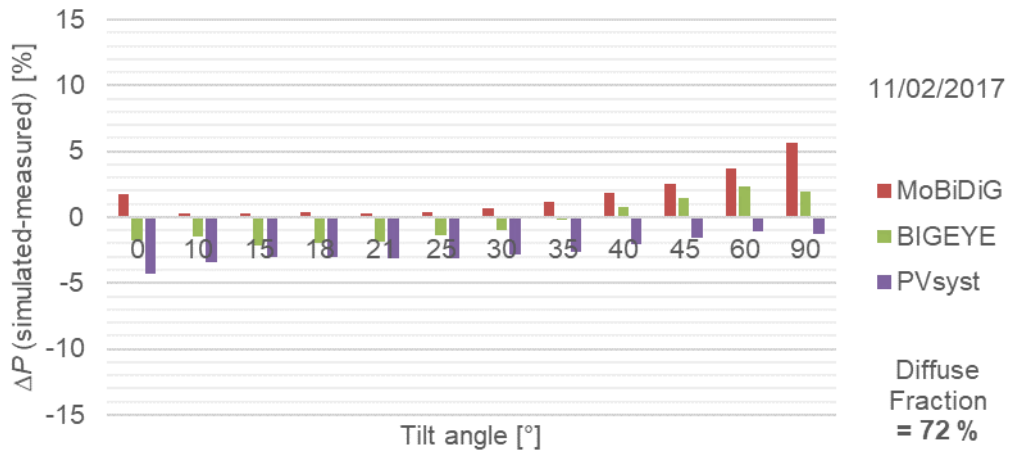
537 The maximum deviation at completely overcast conditions varies for the respective models is
538 below 10 %. The total deviation of all simulations is in a range of about $\pm 10\%$. For conditions with
539 mixed irradiation, the same trends can be observed, however with a lower deviation for the
540 respective models of about 6 % and a total variation of all models of about $\pm 6\%$.

541 It has to be pointed out that the significance of the described pronounced deviations at overcast
542 conditions for the annual yield is limited due to a small contribution to the total yield.

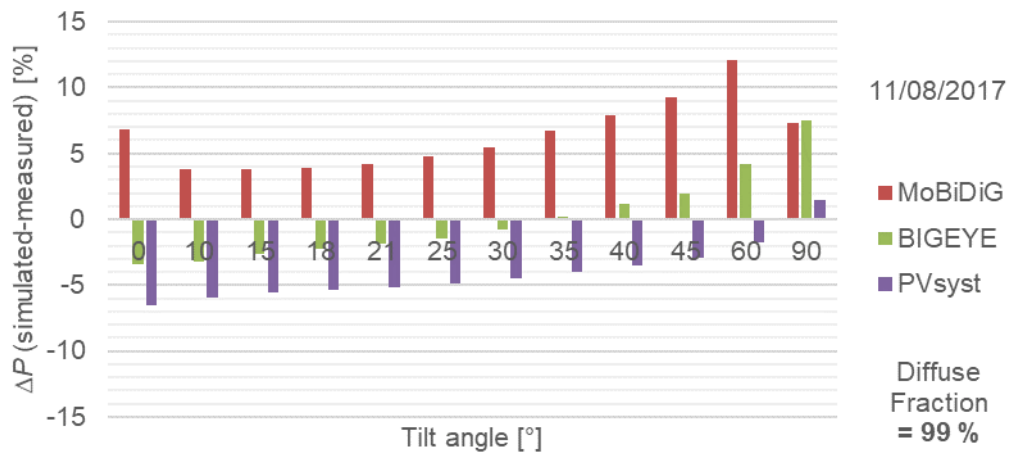
543



544 a)



545 b)



546 c)

547 **Fig. 15.** Deviation, (simulated-measured) to measured, of the total power output at all tilt angles
 548 on all days.

549

550 6. Conclusions

551 The prediction accuracy of three simulation tools was tested with the BIFOROT test rig at varying
552 irradiation conditions and tilt angles. The aim of this work is not a comparison of long-term
553 measurement and simulation data, but the analysis of characteristic trends and dependencies at
554 specific conditions.

555 The simulated front side irradiance is as good as the irradiance data enables. At days with
556 predominantly diffuse light, the results are very sensitive to the small difference between the
557 measured *GHI* and *DHI*. It was demonstrated how small uncertainties in the beam component are
558 enhanced for steeper tilt angles. Even though this affects both mono- and bifacial modules,
559 installations with the latter ones may be more prone to this effect, because the two-sided light-
560 sensitivity allows a wider range of possible tilt angles. Largest deviations of the respective front
561 side irradiation simulations are found for small tilt angles or vertical module orientation. Due to the
562 larger contribution of the front side for south-oriented modules, related effects will dominate the
563 overall accuracy at conditions with low direct irradiation and corresponding orientation.

564 Rear side measurements are more affected by inhomogeneities and shading by the mounting,
565 particularly at conditions with high direct irradiation share. Although all simulation tools showed a
566 good correlation with the rear side current, distinct differences between the three tools were
567 observed. A clear correlation between these differences and the approach used by each tool,
568 however, cannot be made at this stage.

569 The observed trends in bifacial gains and the measured total electrical output are well predicted
570 by all three models. Particularly for conditions with high direct irradiance share, the deviations are
571 remarkably small. In addition, the course over the tilt angles shows a dip for moderate tilt angles.
572 For 30° to 45° the deviation is smaller than $\pm 2\%$ for all models and mostly well below $\pm 1\%$.
573 There is an increase of the deviation towards horizontal and vertical tilt for these irradiation
574 conditions, but the deviation is within $\pm 3\%$.

575 The deviations get larger with decreasing direct irradiance share. Again, the largest deviations of
576 each model are observed for horizontal and vertical tilt. For conditions with low direct irradiation,
577 the course of the deviations shows a similar trend towards steeper tilt angles. There is however
578 an "offset" between the models, the maximum deviation can be found at horizontal or vertical
579 mounting. The maximum deviation at completely overcast conditions varies for the respective
580 models in a range of about 10%. The total deviation of all simulations is in a range of about
581 $\pm 10\%$. For conditions with mixed irradiation, the same trends can be observed with a deviation
582 for the respective models within about 6% and a total variation of all three models of about $\pm 6\%$.

583 Summarized it can be said that the three simulation tools give similar results and are in agreement
584 with the experiment, particularly for conditions with large direct irradiation share. This shows that
585 bifacial yield modeling is reaching a stage of maturity.

586 The prediction accuracy of the annual yield will be in between the extremely good results obtained
587 for clear sky conditions and the ones with larger deviations for overcast days at very low or steep
588 tilt angles. It has to be pointed out that the impact of overcast conditions for the annual yield is
589 limited due to the comparatively small contribution to the total yield. In order to get a good estimate
590 for the yield prediction of an entire year, a larger data set needs to be analyzed, ideally this would
591 be the measurements of one full year.

592 The small number of analyzed days makes it also difficult to study specific differences and trends
593 of the three models. Also here, the analysis of a full year worth of data would allow to obtain more
594 conclusive results. The BIFOROT system is still operating and has collected so far almost two
595 years of data. Our aim is to present the analysis of this data in a future study.

596

597 **Funding sources**

598 The contribution of ISC Konstanz has been funded by the EC (Horizon 2020) and by the German
599 BMWi (FKZ 0324088A) within the Solarera.net project "Bifalo"

600

601 **Appendix**

602 *MoBiDiG simulation parameters*

603 Mid-hour averaged weather and irradiance data have been created for each day and tilt angle.
 604 The ground albedo has been set to 0.51; the axial height of BIFOROT system is set to 0.75 m and
 605 the clearance height has been calculated during the simulation for each tilt angle. The angle of
 606 incidence modifier has been used, considering the front glass has an antireflective coating while
 607 the back glass is without antireflective coating.

Module Length (m)	1.66
Number of Modules per Row	4
Number of Rows	3
AIM_model	physicaliam
Temperature coefficient of power (%/°C)	-0.415
ϕ_{Pmax} (Bifaciality factor, power)	0.78

608 **Table 1:** Input parameters as applied in the simulation with MoBiDiG

609
 610 MoBiDiG calculates the rear irradiance for twelve positions and uses the average for the electrical
 611 output calculation.

612
 613 *BIGEYE simulation parameters*
 614 BIGEYE carried out simulations for all timesteps at all the four days considered. The value of
 615 ground reflection coefficient was 0.51. The geometry of the field included three rows with for
 616 modules, i.e. including the dummy modules on the eastern side of the set-up.

I_L	8.648	A
a	1.683	V ⁻¹
I_0	0.636	nA
R_{series}	0.231	Ω
R_{shunt}	5000	Ω
αI_{sc}	0.0036	A/K
E_{gap} (@STC)	1.12	eV
dE_{gap}/dT	0.0002677	eV/K
ϕ_{Pmax} (Bifaciality factor, power)	0.78	

617 **Table 2:** BIGEYE parameters for the STC 1-diode equation, and additional parameters used for
 618 the I-V temperature/irradiance translation according to (De Soto 2006)

619

$(1-R-T)$ front	0.82	
$(1-R-T)$ rear	0.82	

U_c	50	$Wm^{-2}K^{-1}$
-------	----	-----------------

620 **Table 3:** BIGEYE input parameters for the module thermal model

621
622 BigEye calculates the irradiance on four points in each cell and takes the average over the whole
623 module.

624
625 *PVsyst simulation parameters*

626 The measured data, which comes in one-minute intervals, was averaged, in order to get the hourly
627 steps that are needed as input to the simulation. The simulation was performed with the ‘unlimited
628 sheds’ model that allows a simplified calculation for regularly spaced rows. For the transposition,
629 the Perez model is used. The calculation takes into account the direct and diffuse sky irradiance
630 on the front and backside, including inter-row shadings. Furthermore, it computes the direct and
631 diffuse irradiance reaching the ground, and the fractions scattered back to the front and rear side
632 of the bifacial modules. For the comparison with pyranometer measurements, the simulated
633 irradiance values do not contain IAM losses, since they do not occur with pyranometers.

634 For the bifacial model, a ground albedo of 51 % was assumed. The height over ground was
635 adapted for each tilt angle, such that the center of the PV module stayed at the height of the
636 rotating axis.

637 The temperature coefficient U_c was taken as $24 W/m^2/K$, which corresponds to a freestanding
638 installation with reduced air circulation. The effect of wind speed was not taken into account.

639 The single diode parameters, which are gathered in a so-called PAN file, are given in the table
640 below.

$I_{sc}(STC)$	8.725	A
μV_{oc}	-115	mV/K
Γ	0.96	
I_{0STC}	0.024	nA
R_{series}	0.265	Ω
R_{shunt}	500	Ω
ϕ_{Pmax} (Bifaciality factor, power)	0.78	

641 **Table 4:** Single diode input parameters as applied in the simulation with PVsyst

642
643 The irradiance distribution on the rear side of the modules is calculated by taking a regularly
644 spaced set of points on the ground for which the total incoming irradiance has been computed
645 before. The rear side irradiance is the weighted sum of these irradiances, where the weight is the
646 view factor of each point towards the entire rear side of the modules. This view factor is the result
647 of a numerical integration over infinitesimal view factors in all directions at the ground point.

649 **References**

- 650 Appelbaum, J., 2016. Bifacial photovoltaic panels field. *Renewable Energy* 85, 338–343.
651 <https://doi.org/10.1016/j.renene.2015.06.050>
- 652 Baumann, T., Klenk, M., Keller, N., Nussbaumer, H., Baumgartner, F.P., 2017. Illumination Homogeneity
653 of Bifacial Systems – Outdoor Measurements with Systematically Varied Installation Conditions.
654 33rd European Photovoltaic Solar Energy Conference and Exhibition; 1605-1609.
655 <https://doi.org/10.4229/eupvsec20172017-5bv.4.28>
- 656 Berrian, D., Libal, J., Klenk, M., Nussbaumer, H. and Kopecek, R., 2019. Performance of Bifacial PV Arrays
657 With Fixed Tilt and Horizontal Single-Axis Tracking: Comparison of Simulated and Measured
658 Data. *IEEE Journal of Photovoltaics*. DOI: 10.1109/JPHOTOV.2019.2924394
- 659 Berrian, D., Libal, J., Glunz, S., 2017. MoBiDiG simulations and LCOE. Presented at the 4th bifi PV
660 workshop, Konstanz, Germany.
- 661 Burgers, A.R., Janssen, G.J.M., Van Aken, B.B., 2018. BIGEYE: Accurate energy yield prediction of bifacial
662 PV systems. Presented at the 5th bifi PV workshop 2018, Denver, USA.
- 663 Castillo-Aguilella, J.E., Hauser, P.S., 2016. Multi-Variable Bifacial Photovoltaic Module Test Results and
664 Best-Fit Annual Bifacial Energy Yield Model. *IEEE Access* 4, 498–506.
665 <https://doi.org/10.1109/ACCESS.2016.2518399>
- 666 Chiodetti, M., Kang, J., Reise, C., Lindsay, A., 2018. Predicting Yields of Bifacial PV Power Plants – What
667 Accuracy Is Possible? 35th European Photovoltaic Solar Energy Conference and Exhibition; 1623-
668 1629 7 pages, 11399 kb. <https://doi.org/10.4229/35theupvsec20182018-6co.3.4>
- 669 Chudinzow, D., Haas, J., Díaz-Ferrán, G., Moreno-Leiva, S., Eltrop, L., 2019. Simulating the energy yield of
670 a bifacial photovoltaic power plant. *Solar Energy* 183, 812–822.
671 <https://doi.org/10.1016/j.solener.2019.03.071>
- 672 Dassler, D., 2017. Bifacial gain simulations of modules and systems under desert conditions. Presented at
673 the 4th bifi PV workshop, Konstanz, Germany.
- 674 De Soto, W., Klein, S.A., Beckman, W.A., 2006. Improvement and validation of a model for photovoltaic
675 array performance. *Solar Energy* 80, 78–88. <https://doi.org/10.1016/j.solener.2005.06.010>
- 676 Deline, C., Marion, B., MacAlpine, S., Stein, J., Toor, F., Ayala, S., 2017. Bifacial PV Performance Models:
677 Comparison and Field Results. Presented at the 4th bifi PV workshop, Konstanz, Germany.
- 678 DiOrio, N., Deline, C., 2018. Bifacial simulation in SAM. Presented at the 5th bifi PV workshop, Denver,
679 USA.
- 680 Faturrochman, G.J., de Jong, M.M., Santbergen, R., Folkerts, W., Zeman, M., Smets, A.H.M., 2018.
681 Maximizing annual yield of bifacial photovoltaic noise barriers. *Solar Energy* 162, 300–305.
682 <https://doi.org/10.1016/j.solener.2018.01.001>
- 683 Gali, R.S.R., 2017. Energy Yield Model for Bifacial PV Systems: A study and analysis of temperature & rear
684 irradiance models (Master Thesis). TU Delft, Delft.
- 685 Guerrero-Lemus, R., Vega, R., Kim, T., Kimm, A., Shephard, L.E., 2016. Bifacial solar photovoltaics – A
686 technology review. *Renewable and Sustainable Energy Reviews* 60, 1533–1549.
687 <https://doi.org/10.1016/j.rser.2016.03.041>
- 688 Guo, S., Walsh, T.M., Peters, M., 2013. Vertically mounted bifacial photovoltaic modules: A global
689 analysis. *Energy* 61, 447–454. <https://doi.org/10.1016/j.energy.2013.08.040>
- 690 Hansen, C.W., Riley, D.S., Deline, C., Toor, F., Stein, J.S., 2017. A Detailed Performance Model for Bifacial
691 PV Modules. 33rd European Photovoltaic Solar Energy Conference and Exhibition; 2395-2400 6
692 pages, 4395 kb. <https://doi.org/10.4229/eupvsec20172017-6bv.2.35>
- 693 Hansen, C.W., Stein, J.S., Deline, C., MacAlpine, S., Marion, B., Asgharzadeh, A., Toor, F., 2016. Analysis of
694 irradiance models for bifacial PV modules, in: 2016 IEEE 43rd Photovoltaic Specialists Conference
695 (PVSC). Presented at the 2016 IEEE 43rd Photovoltaic Specialists Conference (PVSC), pp. 0138–
696 0143. <https://doi.org/10.1109/PVSC.2016.7749564>

697 Ishikawa, N., 2016. World First Large Scale 1.25MW Bifacial PV Power Plant on Snowy Area in Japan.
698 Presented at the 3rd bifi PV workshop, Myazaki, Japan.

699 Janssen, G.J.M., Burgers, A.R., Binani, A., Carr, A.J., Van Aken, B.B., Romijn, I.G., Klenk, M., Nussbaumer,
700 H., Baumann, T., 2018. How to Maximize the kWh/kWp Ratio: Simulations of Single-Axis Tracking
701 in Bifacial Systems. 35th European Photovoltaic Solar Energy Conference and Exhibition; 1573-
702 1577. <https://doi.org/10.4229/35thepvsec20182018-6bo.7.5>

703 Janssen, G.J.M., Tool, K.C.J., Kossen, E.J., Van Aken, B.B., Carr, A.J., Romijn, I.G., 2017. Aspects of bifacial
704 cell efficiency. *Energy Procedia* 124, 76–83. <https://doi.org/10.1016/j.egypro.2017.09.334>

705 Janssen, G.J.M., Van Aken, B.B., Carr, A.J., Mewe, A.A., 2015. Outdoor Performance of Bifacial Modules
706 by Measurements and Modelling. *Energy Procedia* 77, 364–373.
707 <https://doi.org/10.1016/j.egypro.2015.07.051>

708 João, G., 2013. Testing bifacial PV cells in symmetric and asymmetric concentrating CPC collectors.
709 *Engineering* 05, 185–190. <https://doi.org/10.4236/eng.2013.51B034>

710 Klenk, M., 2018. Bifacial modeling with the BIFOROT. Presented at the 5th bifi PV workshop, Denver,
711 USA.

712 Klenk, M., 2017. BIFOROT –Experimental data for LCOE appraisal of bifacial systems. Presented at the 4th
713 bifi PV workshop, Konstanz, Germany.

714 Kopecek, R., Libal, J., 2018. Towards large-scale deployment of bifacial photovoltaics. *Nature Energy* 3,
715 443–446. <https://doi.org/10.1038/s41560-018-0178-0>

716 Kreinin, L., Bordin, N., Karsenty, A., Drori, A., Grobgeld, D., Eisenberg, N., 2010. PV module power gain
717 due to bifacial design. Preliminary experimental and simulation data, in: 2010 35th IEEE
718 Photovoltaic Specialists Conference. Presented at the 2010 35th IEEE Photovoltaic Specialists
719 Conference, pp. 002171–002175. <https://doi.org/10.1109/PVSC.2010.5615874>

720 Kreuzmann, A., 2017. Eine Insel mit zwei Bergen. *Photon Juni / 6*, 30–32.

721 Kunath, L., 2017. Enhanced energy yield for PV systems using bifacial modules: simulation and model
722 verification. Presented at the 4th bifi PV workshop, Konstanz, Germany.

723 Lamers, M.W.P.E., Özkalay, E., Gali, R.S.R., Janssen, G.J.M., Weeber, A.W., Romijn, I.G., Van Aken, B.B.,
724 2018. Temperature effects of bifacial modules: Hotter or cooler? *Solar Energy Materials and*
725 *Solar Cells* 185, 192–197. <https://doi.org/10.1016/j.solmat.2018.05.033>

726 Liang, T.S., Praveettoni, M., Deline, C., Stein, J.S., Kopecek, R., Singh, J.P., Luo, W., Wang, Y., Aberle, A.G.,
727 Khoo, Y.S., 2019. A review of crystalline silicon bifacial photovoltaic performance
728 characterisation and simulation. *Energy & Environmental Science* 12, 116–148.
729 <https://doi.org/10.1039/C8EE02184H>

730 Libal, J., Kopecek, R., 2018. Bifacial Photovoltaics: Technology, Applications and Economics, *Energy*
731 *Engineering*. IET Institution of Engineering and Technology.

732 Lim, Y.S., Lo, C.K., Kee, S.Y., Ewe, H.T., Faidz, A.R., 2014. Design and evaluation of passive concentrator
733 and reflector systems for bifacial solar panel on a highly cloudy region – A case study in Malaysia.
734 *Renewable Energy* 63, 415–425. <https://doi.org/10.1016/j.renene.2013.10.008>

735 Lindsay, A., Chiodetti, M., Binesti, D., Mousel, S., Lutun, E., Radouane, K., Bermes, S., Lecussan, R., 2016a.
736 Enhanced Bifacial PV Modelling With Ray-Tracing. Presented at the 6th PV PMC Workshop,
737 Freiburg, Germany.

738 Lindsay, A., Chiodetti, M., Binesti, D., Mousel, S., Lutun, E., Radouane, K., Christopherson, J., 2016b.
739 Modelling of Single-Axis Tracking Gain for Bifacial PV Systems. 32nd European Photovoltaic Solar
740 Energy Conference and Exhibition; 1610-1617 8 pages, 11913 kb.
741 <https://doi.org/10.4229/eupvsec20162016-5co.14.2>

742 Marion, B., MacAlpine, S., Deline, C., Asgharzadeh, A., Toor, F., Riley, D., Stein, J., Hansen, C., 2017. A
743 Practical Irradiance Model for Bifacial PV Modules, in: 2017 IEEE 44th Photovoltaic Specialist
744 Conference (PVSC). Presented at the 2017 IEEE 44th Photovoltaic Specialists Conference (PVSC),
745 IEEE, Washington, DC, pp. 1537–1542. <https://doi.org/10.1109/PVSC.2017.8366263>

746 Mermoud, A., Wittmer, B., 2018a. Horizontal Axis Trackers with Bifacial Modules in PVsyst. Presented at
747 the 2018 10th PV Performance Modeling Workshop, Albuquerque, USA.

748 Mermoud, A., Wittmer, B., 2018b. Bifacial, PV System, Simulation, Tracking, Modelling / Modeling,
749 Modelling and Simulation. Presented at the 35th European Photovoltaic Solar Energy Conference
750 and Exhibition, Amsterdam, pp. 1929–1934. <https://doi.org/10.4229/35thEUPVSEC20182018-6CV.2.19>

751

752 Mermoud, A., Wittmer, B., 2017. Bifacial shed simulations with PVsyst. Presented at the 4th bifi PV
753 workshop, Konstanz, Germany.

754 Meydbray, J., 2018. Barriers to Financing Bifacial PV Projects. Presented at the 5th bifi PV workshop,
755 Denver, USA.

756 Nordmann, T., Vontobel, T., Clavadetscher, L., 2012. 15 years of practical experience in development and
757 improvement of bifacial photovoltaic noise barriers along highways and railway lines in
758 Switzerland, in: Proceedings to the 27th European Photovoltaic Solar Energy Conference.
759 Presented at the 27th European Photovoltaic Solar Energy Conference, pp. 3843–3847.

760 Nussbaumer, H., Klenk, M., Halm, A., Schneider, A., 2018. State-of-the-art bifacial module technology.
761 Photovoltaics International 41, 108–125.

762 Nussbaumer, H., Klenk, M., Morf, M., Keller, N., 2019. Energy yield prediction of a bifacial PV system with
763 a miniaturized test array. Solar Energy 179, 316–325.
764 <https://doi.org/10.1016/j.solener.2018.12.042>

765 Obara, S., Konno, D., Utsugi, Y., Morel, J., 2014. Analysis of output power and capacity reduction in
766 electrical storage facilities by peak shift control of PV system with bifacial modules. Applied
767 Energy 128, 35–48. <https://doi.org/10.1016/j.apenergy.2014.04.053>

768 Osborne, M., 2017. SNEC 2017: The next big solar module trend on display [WWW Document]. PV Tech.
769 URL [https://www.pv-tech.org/editors-blog/snec-2017-the-next-big-solar-module-trend-on-](https://www.pv-tech.org/editors-blog/snec-2017-the-next-big-solar-module-trend-on-display)
770 [display](https://www.pv-tech.org/editors-blog/snec-2017-the-next-big-solar-module-trend-on-display) (accessed 5.9.19).

771 Pelaez, S.A., Deline, C., MacAlpine, S.M., Marion, B., Stein, J.S., Kostuk, R.K., 2019. Comparison of Bifacial
772 Solar Irradiance Model Predictions With Field Validation. IEEE Journal of Photovoltaics 9, 82–88.
773 <https://doi.org/10.1109/JPHOTOV.2018.2877000>

774 Perez, R., Ineichen, P., Seals, R., Michalsky, J., Stewart, R., 1990. Modeling daylight availability and
775 irradiance components from direct and global irradiance. Solar Energy 44, 271–289.
776 [https://doi.org/10.1016/0038-092X\(90\)90055-H](https://doi.org/10.1016/0038-092X(90)90055-H)

777 Perez, R., Seals, R., Ineichen, P., Stewart, R., Menicucci, D., 1987. A new simplified version of the perez
778 diffuse irradiance model for tilted surfaces. Solar Energy 39, 221–231.
779 [https://doi.org/10.1016/S0038-092X\(87\)80031-2](https://doi.org/10.1016/S0038-092X(87)80031-2)

780 Perez, R., Seals, R., Michalsky, J., 1993. All-weather model for sky luminance distribution—Preliminary
781 configuration and validation. Solar Energy 50, 235–245. [https://doi.org/10.1016/0038-](https://doi.org/10.1016/0038-092X(93)90017-1)
782 [092X\(93\)90017-1](https://doi.org/10.1016/0038-092X(93)90017-1)

783 Reise, C., Schmid, A., 2015. Realistic Yield Expectations for Bifacial PV Systems – An Assessment of
784 Announced, Predicted and Observed Benefits. 31st European Photovoltaic Solar Energy
785 Conference and Exhibition; 1775-1779 5 pages, 2706 kb.
786 <https://doi.org/10.4229/eupvsec20152015-5co.14.6>

787 Romijn, I.G., 2017. Bifacial solar cells-a brief overview. Presented at the 4th bifi PV workshop, Konstanz,
788 Germany.

789 Ross, R.G., Smokler, M.I., 1986. Flat-plate solar array project. Final report-Vol. VI. Engineering sciences
790 and reliability. Report DOE/JPL-1012-125 [WWW Document]. URL
791 <https://authors.library.caltech.edu/15040/1/JPLPub86-31volVI.pdf> (accessed 5.14.19).

792 Shoukry, I., 2015. Bifacial Modules-Simulation and Experiment (Master Thesis). University of Stuttgart,
793 Stuttgart, Germany.

794 Shoukry, I., Libal, J., Kopecek, R., Wefringhaus, E., Werner, J., 2016. Modelling of Bifacial Gain for Stand-
795 alone and in-field Installed Bifacial PV Modules. Energy Procedia 92, 600–608.
796 <https://doi.org/10.1016/j.egypro.2016.07.025>
797 Solarworld [WWW Document], 2016. . Calculating the additional energy yield of bifacial solar modules.
798 URL
799 [https://www.google.de/url?sa=t&rct=j&q=&esrc=s&source=web&cd=4&ved=2ahUKEwiSx7u44Y7iAhUQLFAKHVH_A2QQFjADegQIAhAC&url=http%3A%2F%2Fwww.solarworld-](https://www.google.de/url?sa=t&rct=j&q=&esrc=s&source=web&cd=4&ved=2ahUKEwiSx7u44Y7iAhUQLFAKHVH_A2QQFjADegQIAhAC&url=http%3A%2F%2Fwww.solarworld-usa.com%2F%2Fmedia%2Fwww%2Ffiles%2Fwhite-papers%2Fcalculating-additional-energy-yield-through-bifacial-solar-technology-sw9002us.pdf&usg=AOvVaw3-__DT_AKnBcRHUS6weiUQ)
800 [usa.com%2F%2Fmedia%2Fwww%2Ffiles%2Fwhite-papers%2Fcalculating-additional-energy-](https://www.google.de/url?sa=t&rct=j&q=&esrc=s&source=web&cd=4&ved=2ahUKEwiSx7u44Y7iAhUQLFAKHVH_A2QQFjADegQIAhAC&url=http%3A%2F%2Fwww.solarworld-usa.com%2F%2Fmedia%2Fwww%2Ffiles%2Fwhite-papers%2Fcalculating-additional-energy-yield-through-bifacial-solar-technology-sw9002us.pdf&usg=AOvVaw3-__DT_AKnBcRHUS6weiUQ)
801 [yield-through-bifacial-solar-technology-sw9002us.pdf&usg=AOvVaw3-__DT_AKnBcRHUS6weiUQ](https://www.google.de/url?sa=t&rct=j&q=&esrc=s&source=web&cd=4&ved=2ahUKEwiSx7u44Y7iAhUQLFAKHVH_A2QQFjADegQIAhAC&url=http%3A%2F%2Fwww.solarworld-usa.com%2F%2Fmedia%2Fwww%2Ffiles%2Fwhite-papers%2Fcalculating-additional-energy-yield-through-bifacial-solar-technology-sw9002us.pdf&usg=AOvVaw3-__DT_AKnBcRHUS6weiUQ)
802 Soria, B., Gerritsen, E., Lefillastre, P., Broquin, J.-E., 2016. A study of the annual performance of bifacial
803 photovoltaic modules in the case of vertical facade integration. Energy Science & Engineering 4,
804 52–68. <https://doi.org/10.1002/ese3.103>
805 Stein, J.S., Riley, D., Lave, M., Hansen, C., Deline, C., Toor, F., 2017. Outdoor Field Performance from
806 Bifacial Photovoltaic Modules and Systems [WWW Document]. URL
807 <https://www.osti.gov/servlets/purl/1457637>
808 Sugibuchi, K., Ishikawa, N., Obara, S., 2013. Bifacial-PV Power Output Gain in the Field Test Using
809 “EarthON” High Bifaciality Solar Cells. 28th European Photovoltaic Solar Energy Conference and
810 Exhibition; 4312–4317 6 pages, 9810 kb. <https://doi.org/10.4229/28theupvsec2013-5bv.7.72>
811 Van Aken, B., 2016. Bifacial Modelling – review. Presented at the 3rd bifi PV workshop, Myiazaki, Japan.
812 Van Aken, B.B., Jansen, M.J., Carr, A.J., Janssen, G.J., Mewe, A.A., 2014. Relation between indoor flash
813 testing and outdoor performance of bifacial modules, in: 29th European Photovoltaic Solar
814 Energy Conference, Amsterdam.
815 VDMA-PV, 2019. ITRPV International Technology Roadmap for Photovoltaic [WWW Document]. ITRPV
816 2019. URL <https://itrpv.vdma.org/en/ueber-uns>
817 Veschetti, Y., 2016. Review on bifacial cells. Presented at the bifi PV workshop, Miyazaki, Japan.
818 Wang, S., Wilkie, O., Lam, J., Steeman, R., Zhang, W., Khoo, K.S., Siong, S.C., Rostan, H., 2015. Bifacial
819 Photovoltaic Systems Energy Yield Modelling. Energy Procedia 77, 428–433.
820 <https://doi.org/10.1016/j.egypro.2015.07.060>
821 Yusufoglu, U.A., Pletzer, T.M., Koduvelikulathu, L.J., Comparotto, C., Kopecek, R., Kurz, H., 2015. Analysis
822 of the Annual Performance of Bifacial Modules and Optimization Methods. IEEE Journal of
823 Photovoltaics 5, 320–328. <https://doi.org/10.1109/JPHOTOV.2014.2364406>
824
825